MICROFLUIDIC-BASED FABRICATION OF PHOTONIC MICROLASERS

FOR BIOMEDICAL APPLICATIONS

Omar Cavazos

Thesis Prepared for the Degree of

MASTER OF SCIENCE

UNIVERSITY OF NORTH TEXAS

December 2019

APPROVED:

Maurizio Manzo, Major Professor
Hector R. Siller, Committee Member
Huseyin Bostanci, Committee Member
Seifollah Nasrazadani, Interim Chair of the Department of Engineering Technology
Hanchen Huang, Dean of the College of Engineering
Victor Prybutok, Dean of the Toulouse Graduate School

Cavazos, Omar. *Microfluidic-Based Fabrication of Photonic Microlasers for Biomedical Applications*. Master of Science (Engineering Technology), December 2019, 62 pp., 2 tables, 51 figures, 2 appendices, 80 numbered references.

Optical microlasers have been used in different engineering fields and for sensing various applications. They have been used in biomedical fields in applications such as for detecting protein biomarkers for cancer and for measuring biomechanical properties. The goal of this work is to propose a microfluidic-based fabrication method for fabricating optical polymer based microlasers, which has advantages, over current methods, such us the fabrication time, the contained cost, and the reproducibility of the microlaser's size. The microfluidic setup consisted of microfluidic pumps and a flow focusing droplet generator chip made of polydimethylsiloxane (PDMS). Parameters such as the flow rate (Q) and the pressure (P) of both continuous and dispersed phases are taken into account for determining the microlaser's size and a MATLAB imaging tool is used to reduce the microlaser's diameter estimation. In addition, two applications are discussed: i) electric field measurements via resonator doped with Di-Anepps-4 voltage sensitive dye, and ii) strain measurements in a 3D printed bone-like structure to mimic biomedical implantable sensors.

ACKNOWLEDGEMENT

First, I would like to give special thanks to my major professor Dr. Manzo for his support and guidance to complete my thesis. He always motivated me to complete my thesis and provided guidance. Also, I would like to thank all my committee members Dr. Bostanci and Dr. Siller for their support and guidance for the completion of my thesis. I also, thank Christopher Haney, Hossain Ahmed, Erick Ramírez-Cedillo, Rick Pierson, and Bobby Grimes for assistance in fabricating components for my thesis. In addition, I thank the engineering technology department for their support while I worked on my thesis.

Lastly, I thank all my friends and family who supported me throughout my completion of my thesis. In addition, I thank my aunt Blanca and my uncle Porfirio for their moral support. Also, I thank my parents Omar and Teresa for their moral support.

TABLE OF CONTENTS

Page

LIST OF TABLES

Page

LIST OF FIGURES

Page

CHAPTER 1

INTRODUCTION

1.1 Motivation

Optical sensors have been a prominent topic of interest in recent years. There is a need for sensing with high sensitivity and resolution. These technologies have been applied for biomedical applications. Optical biosensors have been used for cancer biomarker detection, optical heart monitoring, and biomechanical monitoring [1-5]. Specifically, optical microlasers can open the avenue for highly sensitive sensors for biomedical applications. Biocompatible polymers have been used to fabricate these devices such Polydimethylsiloxane (PDMS) and Polyethylene glycol diacrylate (PEGDA). Therefore, efficient fabrication methods for optical microlasers can reduce the cost of optical microlasers. Therefore, I gained interest in dye-doped microlasers after realizing the potential impact of microlasers impact in different fields of industry. Most, notably dye-doped microlasers can improve on healthcare methods and lead to grounding breaking impact. This is ultimately why I decided to investigate a microfluidic method, which improves the production rate and reproducibility of microlasers. Reproducibility meaning that microlasers can be fabricated with similar physical properties and size. Droplet generator technology allows to create monodispersed particles with similar size in a short of time. The morphology of microlasers is crucial because it impacts laser modes inside microlaser. Thus, being able to fabricate microlasers in a short time with similar properties can lead to the decrease of cost of fabricating microlasers and lead to further breakthroughs for biomedical applications.

1.2 Thesis Scope and Problem Statement

The purpose of this thesis is to propose a microfluidics-based fabrication method of

photonic microlasers, which fills in a gap in fabrication for solid dye-doped microlasers. The contributions of this thesis will expedite the production time of micro lasers and improve reproducibility. One must understand the concept of a microlaser before fabricating them. Therefore, a brief introduction discusses the microlaser theory and different types of current fabrication methods. Then microfluidics is discussed, which defines the bounds for the fabrication method used. In addition, biomedical applications of dye doped microlasers are showed. First, a neurotransducer based on voltage sensitive dye microlasers were introduced. Secondly, microlasers were used for biomechanical testing of a 3-D printed bone-like structures.

1.3 Goals and Objective

The goal for this thesis is to highlight a microfluidic based fabrication method of dye-doped microlasers for biomedical applications. The objectives of this thesis are shown below:

- Discuss the importance of microlasers and microfluidic method
- Fabricate microlasers based on microfluidic method
- Retrieve experimental data for analysis and review

1.4 Thesis Overview

This thesis is arranged in a methodical way. Chapter 1 highlights the essential background and introduction of the thesis. The motivation, thesis scope, goals and objective are also discussed in this chapter. In addition, a literature review on microlasers and different fabrication methods is discussed. Chapter 2 discusses the experimental setups and fabrication procedure. In this chapter, details of the spectroscopy setup are discussed. In addition, the microfluidic setup is discussed. The third chapter shows the basics of microfluidics and droplet generation. This includes information such as theoretical fluid mechanics concepts of microfluidics and

multiphase flow theory behind the fabrication of particles. In addition, methods and results for polydimethylsiloxane (PDMS) chip and glass chip are shown. Chapter 4 discusses the two biomedical applications. Chapter 5 discusses the conclusions and future goals for the work in this thesis. Figure 1-1 shows the general organization of this thesis.

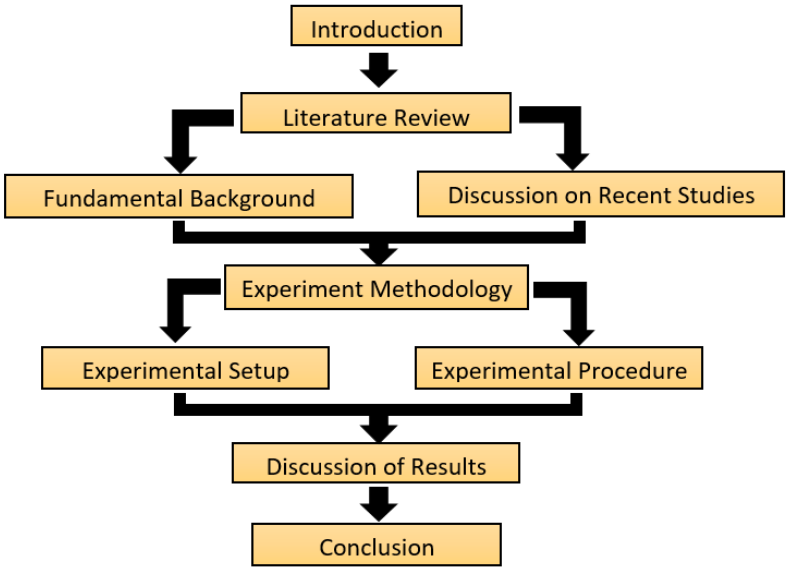

Figure 1-1: Thesis organization.

1.5 Literature Review

1.5.1 Working Principle and Background of Microlasers

Light amplification by stimulated emission of radiation (LASER) is a coherent optical amplifier. A coherent optical amplifier increases the amplitude of the optical field while maintaining its phase [6]. Stimulated emission is when an incoming photon in given laser modes of a specific frequency interacts with an atom in higher energy level, which in turn the electron goes to a lower energy level. The released energy causes a new (clone) photon to be created with a similar phase, frequency, direction, and polarization as the initial photon [7]. As result, the initial

photon and clone photon lead to the emission of additional photons and forward. Figure 1-2 shows the stimulated emission photons.

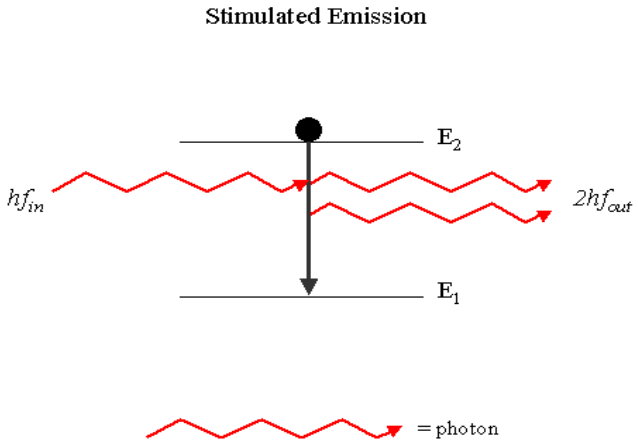

Figure 1-2: Stimulated emission [8].

A gain medium is a medium, which can amplify the power of light [9-10]. The gain medium adds energy to the amplified light by receiving energy by optical pumping. There are different kinds of laser gain media such as laser crystals such as Neodymium-doped yttrium aluminum garnet (Nd:YAG), Ti:Sapphire, and erbium-doped yttrium aluminum garnet (Er: YAG). Most laser dyes are based on organic molecules used in liquid form as solutions. However, solid laser dye resonators have been fabricated with polymer media. Ruby was the first laser material (gain medium) that was observed. Figure 1-3 shows the interior of a ruby laser. The ruby rod is pumped from level 1 to level 3 by the means of a surrounding helical flash lamp. The chromium ions of the ruby are excited to level which they rapidly decay to level 2.

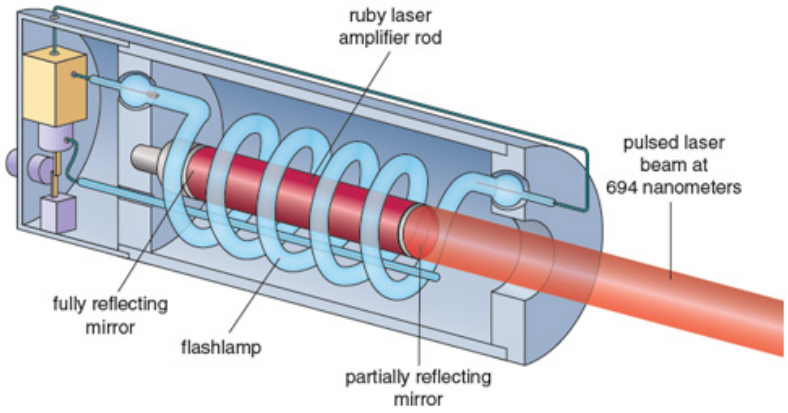

Figure 1-3: Ruby laser [11].

There are different types of laser amplification such as 3 level, 4 level and quasi 3 level as shown in Figure 1-4 as shown from left to right. In a 3 level system, the laser transition occurs in the ground state. A laser transition is a transition between two electronic levels of a laser- active ion [12]. In this transition state, stimulated emission occurs, which leads to optical amplification of laser. In the other hand, in a four level system, the lower level is well above the ground state. The most popular 4 level laser medium is the Nd:YAG. However, quasi 3 level is an intermediate situation, where the lower laser level is really close the ground state [10].

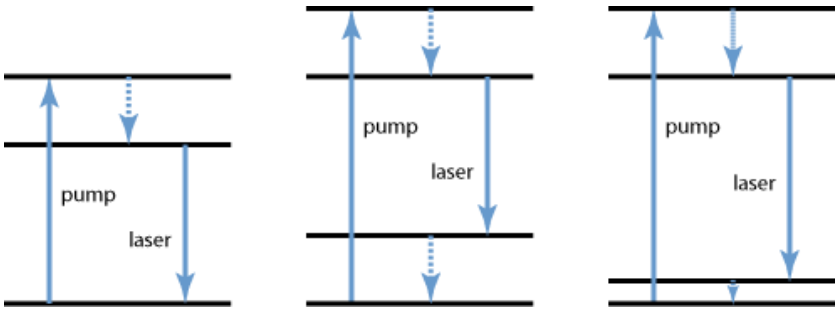

Figure 1-4: Left to right: 3 level, 4 level, quasi 3 level [10].

Dye-doped microresonators act as small lasers, which pass the lasing threshold. The laser dye serves as the gain medium and the whispering gallery cavity serves as the cavity for laser amplification. An external light source excites the optical modes and the fluorescence of the dye as shown Figure 1-5.

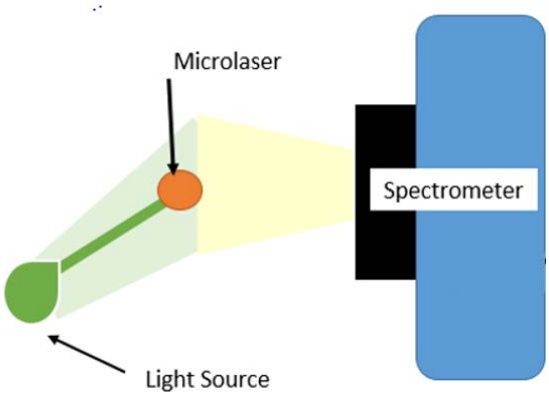

Figure 1-5: Microlaser principle schematic.

Therefore, the dye's fluorescence couples with the optical modes or resonances. The optical resonances or laser modes appear in the emission spectrum, which can be monitored by using a spectrometer. By keeping track of the optical shift, a physical quantity can be measured [13,14]. In this case, the cavity is sphere which allows for laser modes to be present as whispering gallery modes. The whispering gallery mode was discovered by Lord Rayleigh in 20th century in St. Paul's cathedral in London, England. It was observed that a whisper can be heard near walls of the dome but not at the center of the dome. Figure 1-6 shows the dome of St. Paul's Cathedral.

Figure 1-6: Dome of St. Paul's Cathedral [15].

The phenomenon is due to the total internal reflection of acoustic waves inside the walls of the dome [14]. In the application of optical resonators, light electromagnetic waves propagate

inside a dielectric cavity through total internal reflection as shown in Figure 1-7 [16,17]. n_1 and n_2 are the index of refraction of cavity and air respectively.

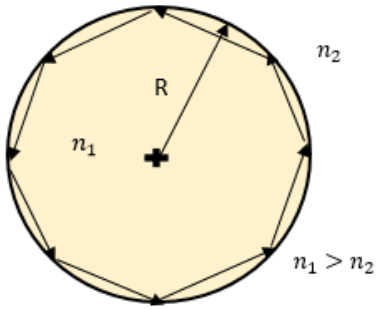

Figure 1-7: WGM cavity schematic.

Overall, spherical, toroidal, cylindrical and disk shapes are commonly used [17]. The sensing element is a resonator that experiences optical mode, which is induced by a light source. The optical modes in an emission spectrum or showcased as peaks as shown in Figure 1-8.

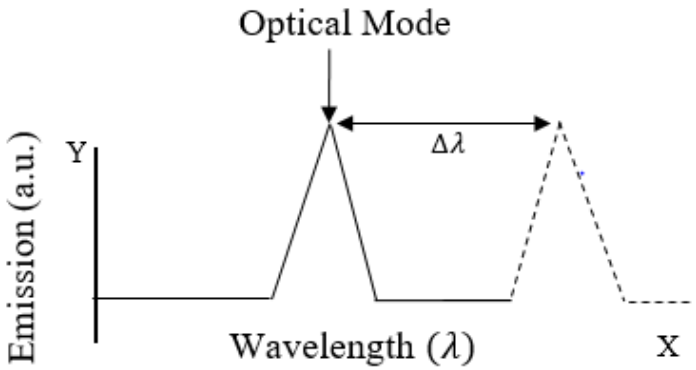

Figure 1-8: Emission spectrum schematic of laser dye-doped optical microlaser.

Whispering gallery mode resonators have a high optical quality factor (Q) or low losses, which makes them suitable optical sensing applications. Due to the high-quality factor the emission spectrum experiences narrow peaks in the graphs due to the narrow linewidth. Quality factor is defined as the resonance (peak) wavelength divided by the linewidth as shown in Equation (1) [18].

$$Q = \frac{\lambda}{\delta\lambda} \tag{1}$$

The spacing between two optical modes or resonances is referred to free spectral range (FSR) as shown in Equation (2) [19].

$$FSR = \frac{\lambda^2}{2\pi nr} \tag{2}$$

In Equation (2), λ is the resonance wavelength, n is the index of refraction of the resonator, and r is the radius of the resonator. Resolution is the smallest possible measurement that a sensor can measure. Any change that effects the optical properties which can lead to shift of the optical modes can be described when the radius R is greater than λ (which is the laser excitation wavelength) by Equation (3) [16].

$$\frac{\Delta R}{R} + \frac{\Delta n_1}{n_1} = \frac{\Delta\lambda}{\lambda} \tag{3}$$

The external loads such as pressure can be detected by monitoring the whispering gallery mode shift in the emission spectrum. The optical resonance condition can be written as [16, 17] Equation (4)

$$2\pi R \approx l\lambda \tag{4}$$

and is valid when R radius of the disk is greater than λ the laser excitation wavelength light in the vacuum. Here n is the refractive index of the disk and l is an integer related to the circumferential node number. The research field is very active and interest of whispering gallery modes is increasing because of their advantages such as high *Q*-factors, low mode volumes, and small size. WGM based sensors have been used in many different applications such as temperature sensors. [18]. Figure 1-9 shows an example of polymeric solid microlaser made with PEGDA monomer and rhodamine B laser dye [19].

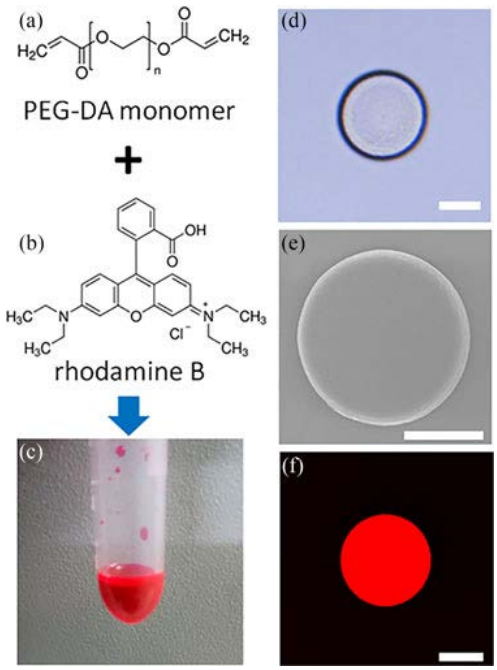

Figure 1-9: (a) Shows formula for PEGDA monomer; (b) shows formula for rhodamine B; (c) polymer/dye mixture composed of 100 uL of PEGDA and 30 uL of rhodamine B aqueous solution; (d) optical microscope image of microdisk microlaser; (e) SEM image of microlaser; (f) two-photon fluorescence microscope images. [19]

However, Ozel et al. implemented hollow core fibers to harness WGM resonator which monitored temperature changes. A novel method was used to create a conical cavity inside the fiber, which served as a fixture for the resonator. The light was then coupled via the hollow core fiber. [20]. WGM based sensors have also been used for fluid mechanic applications as shown by Manzo et al. A latex membrane was used to perturb a WGM resonator in fixed position via fluid flow. The resonators experienced Q factors 10^5 -10^6 [17].

1.5.2 Current Polymeric Microlaser Fabrication Methods

Low cost and great biocompatibility of polymers has increased interest in polymer whispering gallery microcavities [21]. Polymeric photonic devices have eased fabrication and enough use of flexible materials [22]. Therefore, different kinds fabrication methods for this type of structures are discussed. Particles can be fabricated by manually using an optical fiber to form

particles due to gravity at the tip of the fiber [14,23]. Wu et al, developed a method for fabricating a microresonator out of polydimethyl siloxane. It involved dipping an optical fiber in to the PDMS and then forming a sphere at the tip due to surface tension. A laser dye (rhodamine 6 g) was then fused with PDMS in order to enhance the optical resonances of the micro resonator. The resonators then experienced a low threshold at roughly 2.5 $\frac{\mu J}{mm^2}$[23]. In addition, proton beam writing has been used to fabricate dye doped polymer microlasers [24]. Structures made by proton beam writing technique have straight surfaces on sides. WGM structures made by PBW have experienced quality factors of 10^4. Therefore, proton beam writing is a lithographic technique, which high energy protons are focused down to small spot sizes of roughly ~ 100 nm [25]. Vanga et al. fabricated rhodamine B doped SU-8 polymer microlaser by using a PBW method. In this case, a Rhodamine B:SU-8 Polymer mixture was spin coated onto silicon dioxide on a silicon substrate. Then PBW was performed by focusing 2 MeV proton beam on 100 nm spot size, which the beam was then scanned to form geometry [24]. Figure 1-11a shows a scanning electron microscope (SEM) image of the coupled microlaser and Figure 1-11 b shows the comparison of spectral emission of single and coupled microlaser [24].

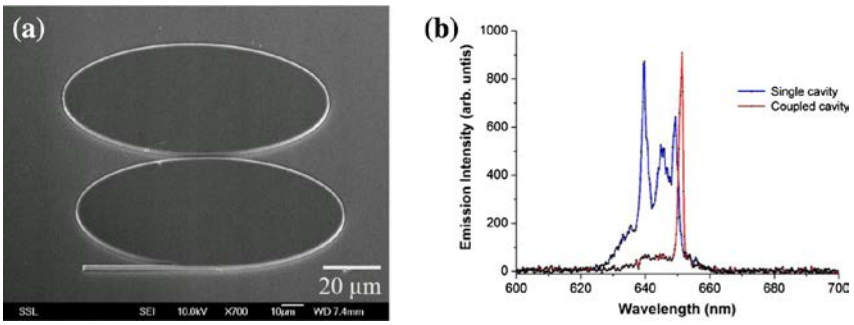

Figure 1-10: (a) SEM of coupled microlaser; (b) spectral emission comparison. Adapted from [24].

Figure 1-10a shows the simulations of end range of photons in SU-8 Photo resist for two different proton energies. Figure 1-10b shows the fabrication procedure of the suspended micro cavities by using proton beam writing with two energies.

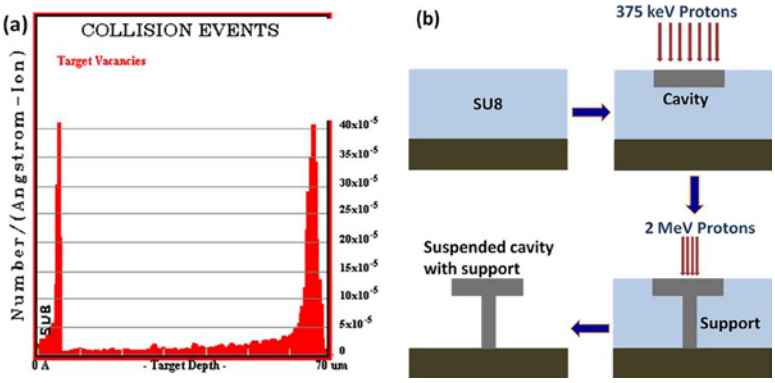

Figure 1-11: (a) End range of photons at 2 different energies; (b) fabrication procedure by proton beam writing. [25]

An advantage of using PBW to fabricate dye doped microlasers with photoresists like SU-8 is that a post baking step is not required. This is notable because polymers tend to degrade at high temperatures. Similarly, a suspending cavity design for a polymer microlaser have been reported by using proton beam writing [26]. Direct laser writing by two-photon polymerization (TPP) has been used with femtosecond lasers to fabricate whispering gallery microcavities [21]. In TPP ultrashort laser beams are tightly focused to a photo sensitive material. Desired 3D shape is possible by moving beam in pattern through selected material. Femtosecond based direct laser writing is also known for having high resolution and generated microcavity with high quality factors [22-27]. Direct UV- Imprinting methods and microring resonator methods have also been reported [28-29]. Microfluidics has also been used to for photonic applications and fluid dye lasers [30-32]. In addition, conjugated-pi polymer lasing microspheres have been fabricated by oil-in-water emulsification method [33]. Microdroplets have been used to fabricate WGM cavities in microfluidic channels. In some cases, microfluidics has been used to control micro

photonic devices at small Reynolds numbers. Currently, droplet generators have been used to fabricate liquid optical microcavities on the chip itself [34-40]. Therefore, this works will fill in the gap for novel polymeric solid microlaser fabrication by microfluidics. Figure 1-12 shows a formation of droplets of an acrylic monomer at a sheath flow junction (flow focusing).

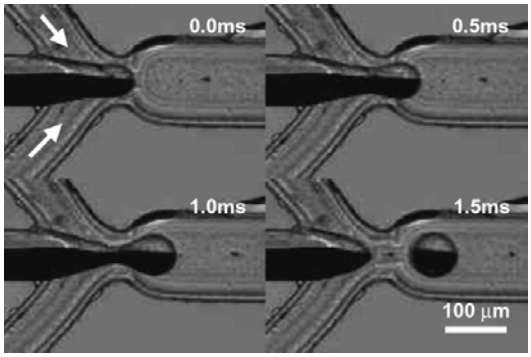

Figure 1-12: Formation of biocolored droplet at sheath-flow junction. Adapted from [35].

CHAPTER 2

EXPERIMENTAL SETUPS

2.1 Microlaser's Input and Output

An external light source excites the optical modes and the fluorescence of the dye used. Therefore, the dye's fluorescence couples with the optical modes. The optical resonances or laser modes appear in the emission spectrum. A Mcpherson Model 209 High resolution spectrometer with a resolution of ~0.017 nm was used to observe the laser modes of the microlasers, which in this case they also the whispering gallery modes. In addition, it has a focal length of 1.33 meter and has a grating groove density of 1800 g/mm [41]. Also, with this grating the spectrometer has a wavelength range of 185-860 nm and a f number of 11.6. A Q-switch Nd:YAG (532 nm) laser with a pulse repetition of 10 Hz, pulse linewidth of 5ns, and beam diameter of ~0.7 cm was used. To get the most light coupled into spectrometer the f number of 11.6 must match with optical elements of the system. Equation (5) is used to solve for the f number where D is the lens diameter and f is the focal length [42]. The diaphragm was used to match F number of the spectrometer to the F number of the optical system (source and lens).

$$\text{F number}(\text{F}/\#) = \frac{D}{f} \tag{5}$$

A charged coupled device (CCD) camera was cooled to (-30℃), which is located at exit slit of the spectrometer. The CCD camera acquisition is trigged by the laser shutter in order to minimize the energy absorbed by microlaser. This avoids optical mode shift due to temperature change. The focal length for convex lens is 25 cm and the diameter is 50.8 mm. Also, Ω is the solid angle. Therefore, the f number for convex lens was found to be ~4.92. In addition, the source (microlaser) is placed at distance twice the focal length of convex lens so at 50 cm. The length b

between diaphragm and lens was ~4.45 cm. Length B' was ~ 45.5 cm. Figure 2–1 shows the lens setup schematic.

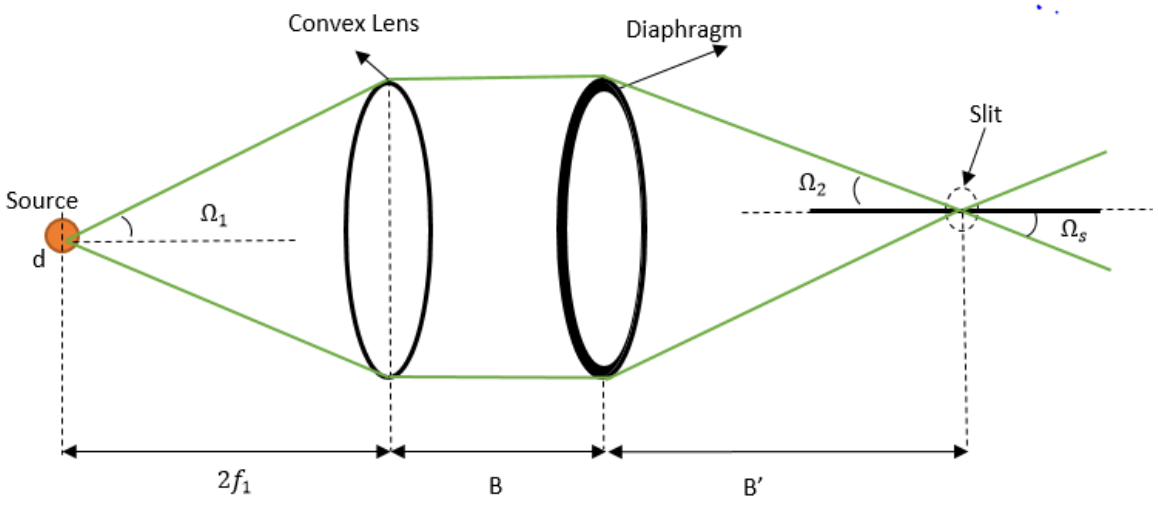

Figure 2-1: Lens setup schematic.

2.2 Microlasers' Fabrication Station

The microfluidic setup consisted of two "Flow EZ" pressure controllers. The pumps are rated for 2000 mbar [43]. One of them is to control fluid flow of the oil. The second pressure controller is used for the polymer/dye mixture. The polymer/dye mixture is used to make particles. In addition, the configuration used for the experiments of this thesis used two pressure feedback modules which allow for automatic adjustment of pressure when adjusting the flowrate of the mineral oil. After the droplets are made from the droplet generator, the microlaser can be cured under a UV lamp. In this study, a 4 watt/365 nm central wavelength UV lamp is used. Figure 2-2 shows the microfluidic setup used for creating particles. The microfluidic chip was placed under the camera microscope in order to view particle production in real time.

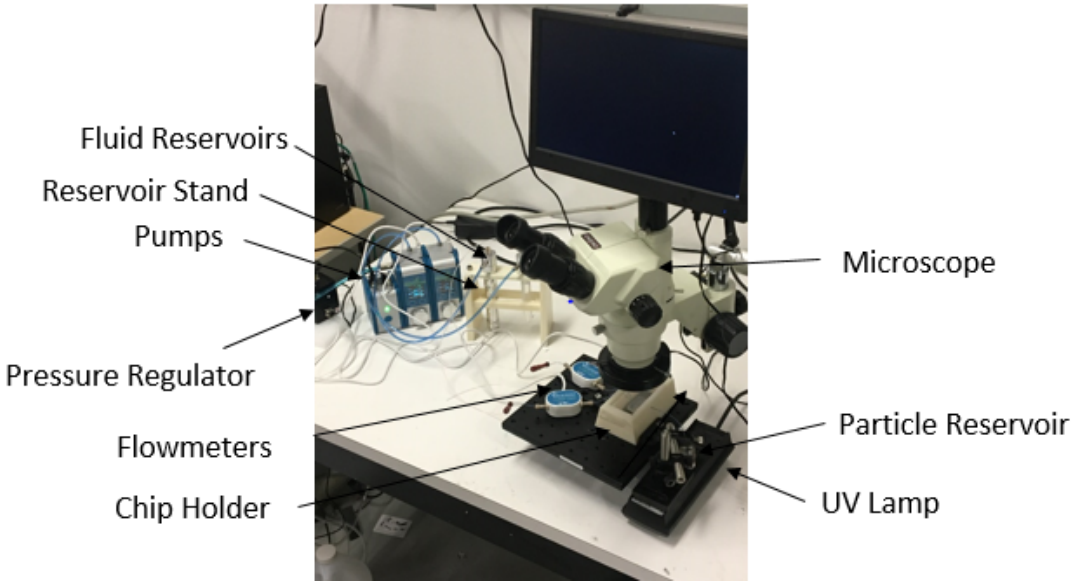

Figure 2-2: Microfluidic experimental setup.

A particle reservoir setup was made by using optical mounts and post to secure outlet tubing to reservoir as shown in Figure 2-3. Also, the guaranteed that the 1/32 inch outer diameter tubing is submerged at all times in order to allow for the proper formation of the microlasers in the glass vile that served as a reservoir.

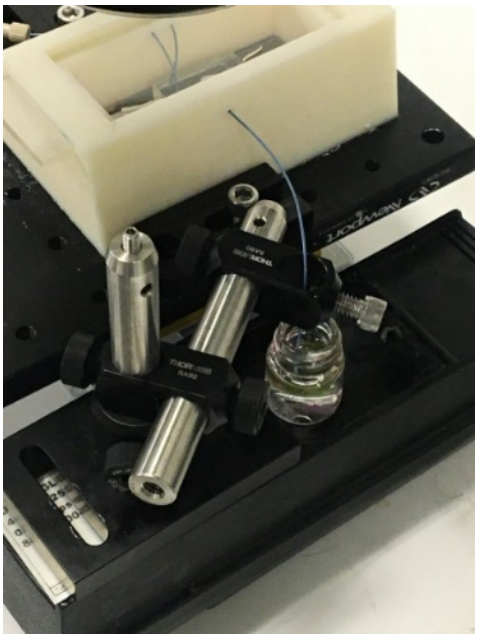

Figure 2-3: Particle reservoir setup.

Figure 2-4: Microfluidic pump.

The pressure pumps are shown in Figure 2-4.The left one is used for the oil phase and the right is used for the aqueous phase. The pump's pressure can be calibrated to zero by pressing the top right button to do so. In addition, the pump for the mineral oil was calibrated for the oil flowrate fluid configuration. However, the polymer/dye mixture pump was calibrated to closet calibration which was for water. This assumption was used since the density of the hydrophilic polymer used (PEGDA) is similar to water. The flow sensors have a resolution of 0.06 μl/min and the fluid reservoirs of the P-Cap type have a working pressure of 7 bar. In addition, the reservoirs used had a capacity of 15 ml [44]. Polyetheretherketone (tubing) of 1/32 inch outer diameter tubing was used to connect the microfluidic system to chip. However, 1/16 inch outer diameter tubing was used to connect pumps to fluid reservoir, which pressurize the reservoirs with air as shown in Figure 2-5.

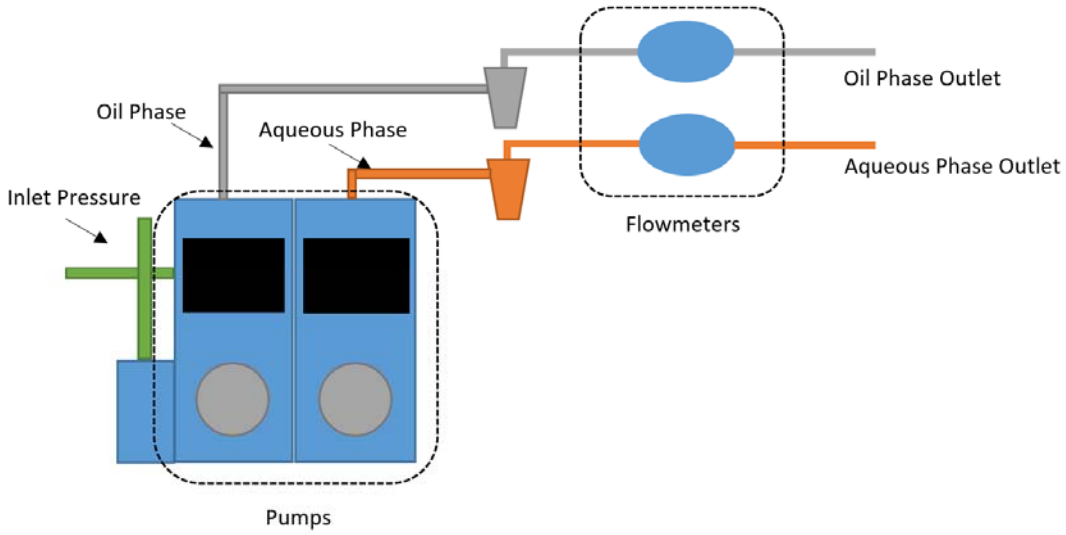

Figure 2-5: Microfluidic schematic.

A custom reservoir rack and mount was designed for the experimental setup. The rack was designed to cover one reservoir, which prevents the polymer-dye mixture from curing. Detailed drawings can be found in Appendix A of this thesis. In addition, a custom microfluidic chip mount was designed for the experimental setup. It was designed so it can secure a standard size microscope slide (75mm x 25mm). The droplet generators used for the experiments were mounted on a microscope slide. This allows securing PDMS chip and glass chip in experiments. It was designed for 1/32 inch tubing connections. Detailed drawings of the microfluidic chip holder can be found in Appendix B of this thesis.

2.3 Data Acquisition Setup

The data acquisition is a crucial part of the experiment procedure. First, the spectrometer was configured properly. It was verified that the “counter” value shown on the spectrometer matched the value of the Andor Solis data acquisition software. This is important because it calibrates the center wavelength of the software as shown in Figure 2-6 for center wavelength of 570 nm.

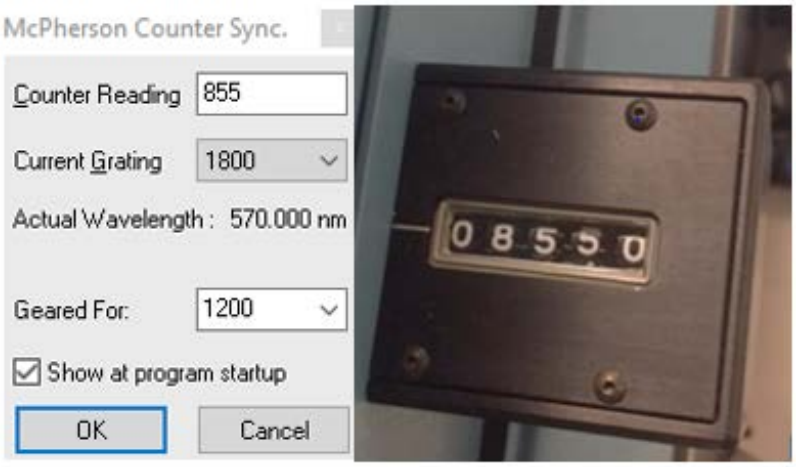

Figure 2-6: Calibration of spectrometer counter.

Also, the CCD camera was kept at -30℃ which increased the signal to noise ratio. Figure 2-7 shows the calibration window for the specified spectrograph used which was the McPherson 209-789 A.

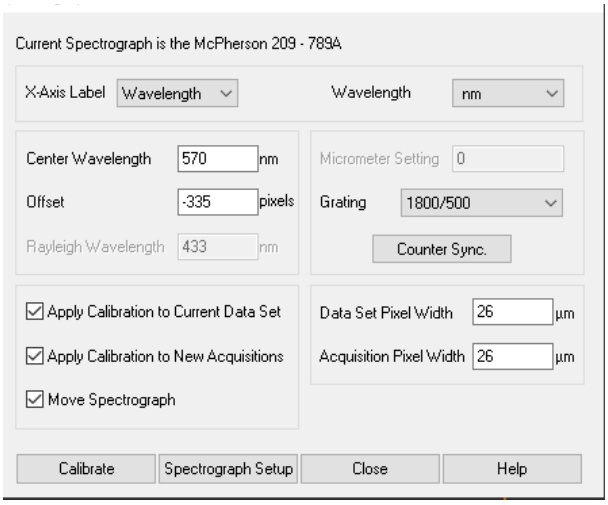

Figure 2-7: Andor Solis calibration interface.

The Andor Solis software is well equipped with embedded tools with the software. For example, one can select a region of interest and determine important specifications at that region. This is very helpful in determining the full width at half maximum (linewidth), which is used to calculate the quality factor. The camera software also comes with external triggering capabilities, which allows the user to acquire date when the laser shutter is pressed on. It also

allows the user to export to different file formats such as asc. The asc file can then be exported into Microsoft Excel for the post processing of data.

CHAPTER 3

FABRICATION OF DYE-DOPED MICROLASERS

3.1 Classical Fabrication Methods

3.1.1 Optical Fiber Gravity/Surface Tension Method

In this section classical methods of optical microlasers are tested. In addition, advantages and disadvantages are emphasized. Figure 3-1 shows the schematic for the optical fiber based fabrication method for microlasers. It is based on gravity and surface tension forces; a segment of optical fiber is dipped into a solution and withdraw from it. Due to the forementioned forces, a spherical particle is formed at the end of the fiber.

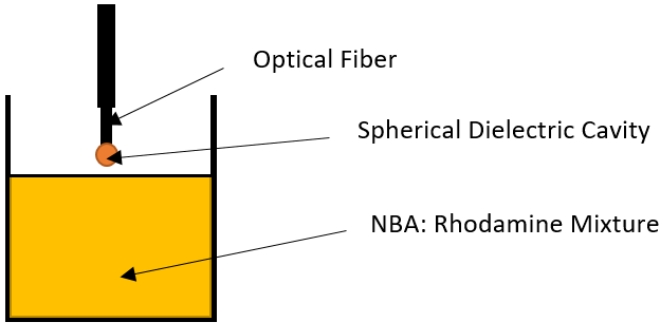

Figure 3-1: Fiber optic based particle fabrication.

The size of particle form is dependent on the velocity that the fiber is extracted from the solution of polymer and laser dye as shown in Figure 3-2. For the experiments performed in the lab, rhodamine 6g laser dye was diluted with ethanol to form a solution with a concentration of ~10^{-4}; the polymer used was Norland Blocking Adhesive (NBA 107).

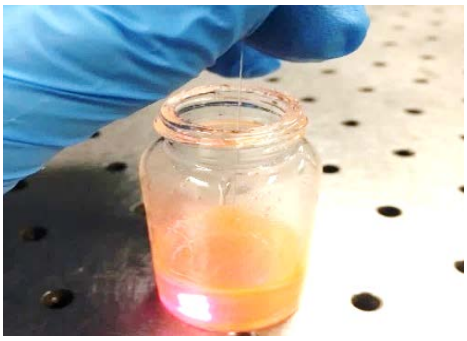

Figure 3-2: Particle fabrication with optical fiber.

The spherical particles were then cured with an ultraviolet lamp with a central wavelength of 365 nm and power of 4 watts. The particles can be cured for ~ 20 min. An example of optical microlaser fabricated by this method is shown in Figure 3-3.

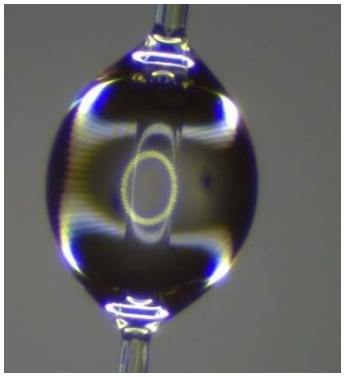

Figure 3-3: Optical microlaser.

One disadvantage of this method is that it is very difficult to fabricate smaller particles ~ smaller than 50 micron. In addition, one can only fabricate one microlaser at a time.

3.1.2 PDMS Suspension Method

Another fabrication method involves suspending particles in PDMS. An optical fiber was used as a tool to transport the polymer/dye mixture to the polydimethylsiloxane (PDMS). The spherical particle was formed when the polymer/dye mixture made contact with the PDMS. This is due to the fact that the polymer/dye mixture does not mix with the PDMS and therefore becomes suspended. This method is more advantageous since it allows several particles to be

fabricated at once as shown in Figure 3-4.

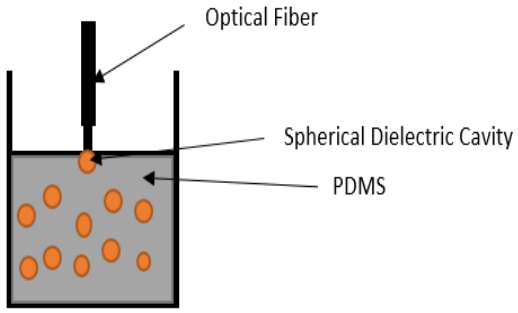

Figure 3-4: Fabrication of suspended particles in PDMS [4].

However, one disadvantage is the extra cleaning procedure used with solvent to remove the PDMS from the microlaser. The particles can be cured with a more powerful 365 nm central wavelength UV lamp (100 watts, 2.5 amps) for ~ 20 minutes. After the particles are cured, the particles are extracted from the glass vile and then cleaned with acetone as shown in Figure 3-5. This method was recorded in [4].

Figure 3-5: Particles fabricated by suspending in PDMS.

3.2 Microfluidic Based Fabrication

3.2.1 Theoretical Background

Microfluidics is the science of devices that deals with amounts of fluids confined in microchannels [45-48]. These microchannels, also known as lab-on-chip systems, have been used

in different applications such as fluid transport, biological applications, and droplet generation. Lab-On-Chip devices combine or integrate laboratory tasks in a chip [47]. Some advantages of microfluidic devices include economic savings, safer handling of chemicals, better multitasking, and high surface-to-volume ratio [45]. Multiphase flows are when two immiscible fluids are flowing in the same channel at the same time. These two fluids are commonly referred to dispersed phase and continuous phase [49].

The continuity equation is shown in Equation (6).

$$\frac{\partial \rho}{\partial t} + \nabla * (\rho \vec{V}) = 0 \tag{6}$$

ρ is density , t is time , and $\vec{V}$ is flow velocity vector field. The momentum equation of fluid motion is the navier-stokes equation, here showed in vector form in Equation (7); ρ is fluid density, $\frac{D}{DT}$ denotes the material derivative for velocity vector $\vec{u}$, p is the applied pressure, and $\vec{f}_B$ denotes any applied body forces [49].

$$\rho \frac{D\vec{u}}{Dt} = -\nabla p + \eta \nabla^2 \vec{u} + \vec{f}_B \tag{7}$$

Applying the no slip condition at the wall (boundary condition), the so called Poiseuille (pressure driven) flow is generated, where a parabolic profile for the velocity distribution is seen for single phase flow as shown in Equation (8) (assuming a long and wide channel). Equation (7) shows the velocity distribution in Poiseuille flow, where n is dynamic viscosity of fluid, $\frac{dp}{dx}$ is pressure gradient, h is channel height.

$$u(y) = \frac{h^2}{2n} \frac{dp}{dx} \left\{ \left(\frac{y}{h}\right)^2 - \left(\frac{y}{h}\right) \right\} \tag{8}$$

The flow rate going through the channel can be found by integrating the velocity profile along the height of the channel as shown in Equation (9) [49]. Where W is width of channel.

$$\dot{Q} = \frac{h^3 W}{12\eta} \frac{dp}{dx} \tag{9}$$

Figure 3-6 shows a schematic for the multiphase flow in fixed channel [50]. Where V is particle velocity and U is continuous phase velocity.

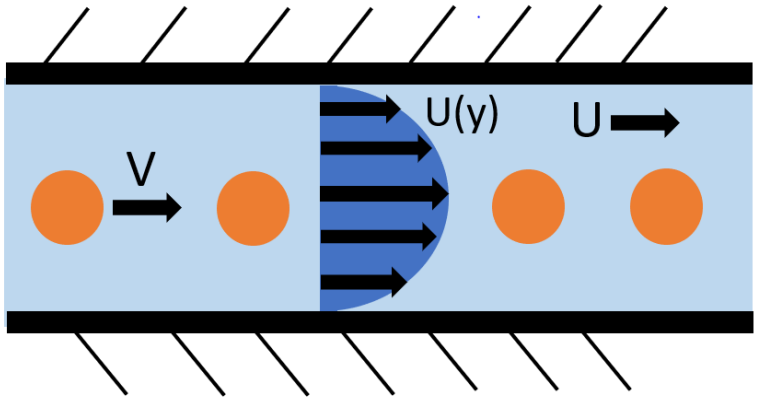

Figure 3-6: Multiphase flow schematic.

As also showed in Figure 3-6 two phases are present: the carrier phase and the dispersed phase. The carrier phase is the fluid which contain the dispersed phase; the dispersed phase is made of droplets. In this case, to solve governing fluid equations (continuity, momentum, and energy for the carrier phase) is necessary to consider additional boundary condition due to the presence of the particles. In addition, microfluidic flows exhibit low Reynolds number (Re < 10). In fact, the Reynolds number is a dimensionless quantity with physical meaning of the ratio of inertia to viscous forces in a fluid and is mathematically defined as Equation (10) [51-53]. This is due to the fact that viscous forces are prominent with the respect inertia forces.

$$Re_d = \frac{\rho V D}{\mu} \tag{10}$$

ρ is the density, V is the velocity of the oil, D is the diameter of particle, and μ is the dynamic viscosity for oil phase. The drag coefficient for particles at low Reynolds number can be calculated with Equation (11).

$$C_D = \frac{24}{Re} \tag{11}$$

The spherical droplet stability in the channel can be analyzed ideally as a force balance between droplet drag force and surface tension as shown in Equation (12). ρ is density of continuous phase , U_c average velocity of continuous phase flow, A_D is cross-sectional area of droplet, C_s is a constant for surface tension, λ is surface tension, and D_i is injection port diameter.

$$\frac{1}{2} C_D \rho U_c^2 A_D = C_s \pi D_i \lambda \tag{12}$$

This case assumes steady state flow, cylindrical channels, and since droplets are microscale, forces such as inertia, momentum force, and buoyancy can be neglected [48]. In addition, the dynamic contact angle made between a flowing oil phase and droplet indicates a balance between viscous forces and capillary forces. This relationship is defined by the capillary number as shown in Equation (13) [46].

$$Ca = \frac{\mu U}{\gamma} \tag{13}$$

Here μ is the dynamic viscosity of the fluid, U is the velocity and γ is the surface tension. This dimensionless number is crucial in determining droplets' break off, which Plateau Raleigh instability leads to droplet detachment. In addition, when contact angle for water based liquid is less than 90 degrees is considered hydrophilic. Hydrophobic is when the opposite scenario occurs when contact is larger than 90 degrees. The contact angle between fluids and droplet generator surface, defines the stability of wetting of continuous phase. Wetting is the ability of a fluid to maintain contact with a surface. In some cases, coatings ensure that a contact angle of more than 90 degrees is present with the aqueous phase [46]. In addition, microdroplets have a small

amount of stored energy, which leads to a clean droplet formation. This is a summation of the E_s is the surface energy and E_k is the kinetic energy as shown in Equation (14).

$$E_d = E_s + E_k \tag{14}$$

Here E_s is the surface energy and E_k is the kinetic energy are shown in equations (15) and (16). Where d_0 is droplet diameter, u is droplet velocity, and λ is surface tension.

$$E_k = \frac{1}{12}\pi\rho d_o^3 u^2 \tag{15}$$

$$E_s = \pi d_o^2 \lambda \tag{16}$$

The weber number is a function of density, surface tension, velocity, and characteristic length as shown in Equation (17). Therefore, it compares fluids inertia to surface tension. In this case, the droplet diameter can be considered as characteristic length [46].

$$We = \frac{\rho u^2 L_{ch}}{\gamma} \tag{17}$$

Equation (18) shows that kinetic energy is less than surface energy. Also, that weber number is proportional to droplet diameter and is a key parameter in determining droplet behavior [48].

$$\frac{E_k}{E_s} = \frac{1}{12} We \tag{18}$$

This dimension less number is crucial in determine in droplet generator in regards to droplet break off. Droplet generation is defined by creating uniform droplets. In addition, monodispersity, size, and shape are crucial parameters in droplet microfluidics [36]. Figure 3-7 shows different types of droplet generators.

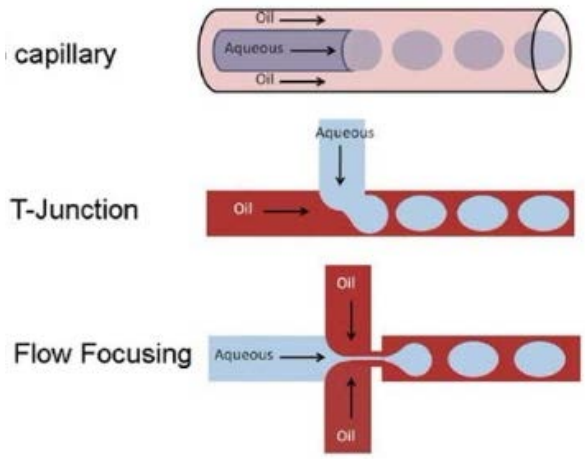

Figure 3-7: Droplet generator types. Adapted from [54].

In droplet generation there 2 main geometries for microfluidic channel. The first case consists of a T-junction in which the continuous phase (oil) is the main channel. The dispersed phase or aqueous phase interests the continuous phase at a ninety degree angle. The shear force and pressure gradient created by continuous phase causes the dispersed phase to thin and then form a droplet [40]. The second type of microfluidic geometry are flow-focusing flow devices. The even or symmetric shear force employed by the continuous phase allows for increased stability of droplet generation. In capillary designs, the dispersed phase is injected, while the continuous phase surrounds the outer edges of capillary. In addition, surfactants such as span 80 can be added to the continuous oil phase in order to avoid coalescence of aqueous droplets. The surfactant reduces the surface tension between oil and aqueous phases [55].

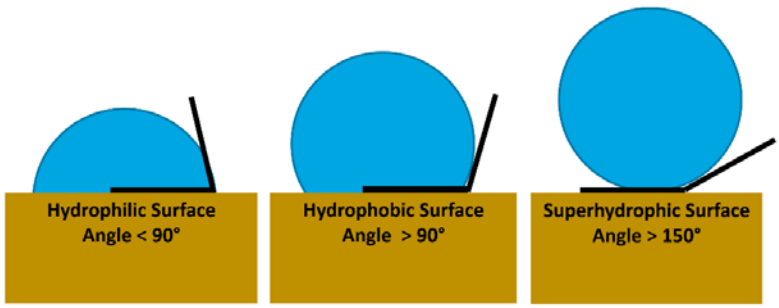

Figure 3-8: Contact angle types for water. [56]

For both T junction and focusing flow junctions the droplet size can be decreased by increasing continuous phase (oil) flow rate. This is because the increase of continuous phase flowrate allows for pinching of the dispersed phase. In other hand, if the dispersed phase flowrate is increased the droplet becomes larger while fixing the continuous phase. In addition, 2 different flow regions in focused flow junctions exist which, are drippling and jetting. The dripping regime occurs due to small flowrates, which causes droplets to be formed right after nozzle. The jetting regime consists of a thread of dispersed phased to be stretched out from nozzle. In addition, the critical weber number of the dispersed phase and critical capillary number of continuous phase distinguish the transition between drippling and regime [48].

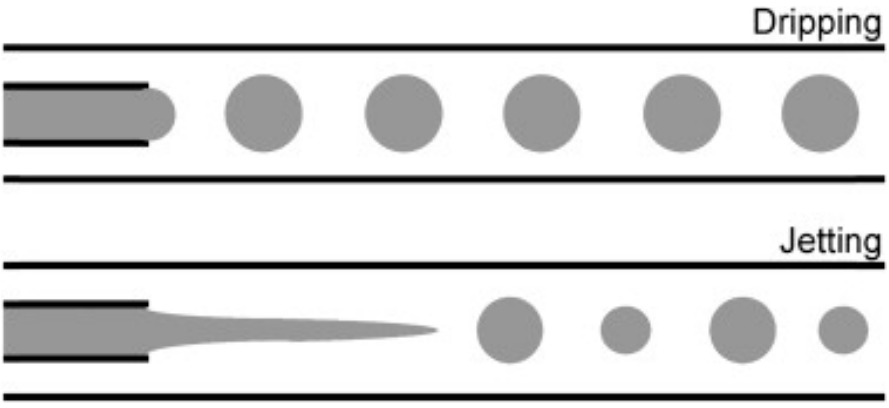

Figure 3-9: Dripping and wetting regimes. [57]

The velocity of outlet channel U_s can be correlated to the spacing Δ and frequency (f) of droplets as shown in Equation (19).

$$U_s = f\Delta \tag{19}$$

The frequency of droplets in flow focusing junctions can be found by Equation (20), which is function of dispersed phase flowrate and droplet volume.

$$Q_i = fV_d \tag{20}$$

3.2.2 Microfluidic Setup Fabrication Procedure

The size of the particles can be adjusted by changing the flow parameters of either the mineral oil or polymer/dye mixture [56]. Generally, the flowrate of the continuous phase is increased in order the make smaller particles. After the droplets are made on the droplet generator, the droplets were cured under a UV lamp. This method allows to fabricate a large number of particles in short period of time.

3.2.3 PDMS Chip

3.2.3.1 Chip Specifications and Preparation

A droplet generator chip made of PDMS was used. Some of the benefits of this chip include surface free coating, visible markers on the PDMS for simple connection. The droplet generator PDMS chip is estimated to make particles at a frequency up to 1200 Hz [58]. Exterior dimensions of the microfluidic chip in millimeters are ~18 mm by 30 mm. This chip uses a flow focusing droplet generator design with a droplet fabrication capability between 15μm to 100 μm.

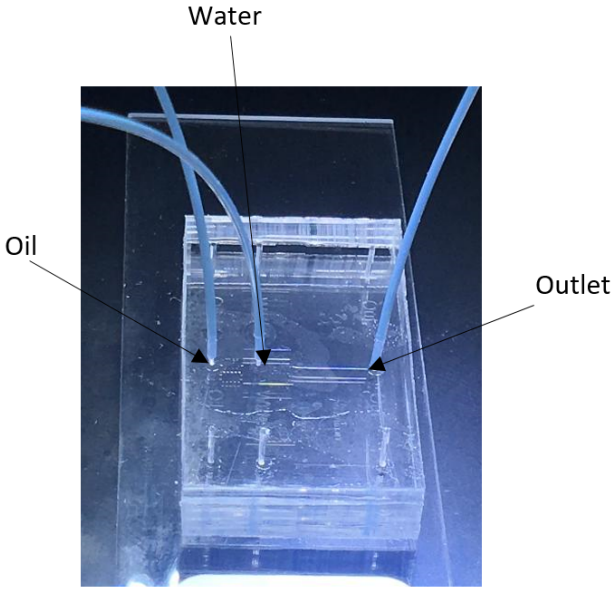

Figure 3-10: PDMS chip.

The size of channel is 200 microns. The outlet was connected to the reservoir, which contained the particles as discussed in chapter 2. The 1/32 inch Peek tubing was connected to microfluidic chip via pushfit. After experiments are conducted, 91 % isopropyl alcohol is used to flush the channels for ~ 30 min at 2000 mbar.

3.2.3.2 Procedures and Experimental Results

The polymer/dye mixture consisted of using PEGDA-700/Rhodamine6-g ($10^{-4} M\ in\ ethanol$) at 4:1 ratio. PEGDA was chosen as the polymer since it is hydrophilic and is compatible with the hydrophobic channel. As discussed previously, a hydrophobic channel allows the generation of hydrophilic only droplets. In addition, PEGDA is a renowned biocompatible material that is used for microlasers such as in [4,19]. The chip was used to create particles ranging from 80 to 150 microns in diameter size. Figure 3-11 shows a photograph of the channel where droplets are visible being generated by using a 4:1 ratio between PEGDA and rhodamine 6G dispersed in mineral oil.

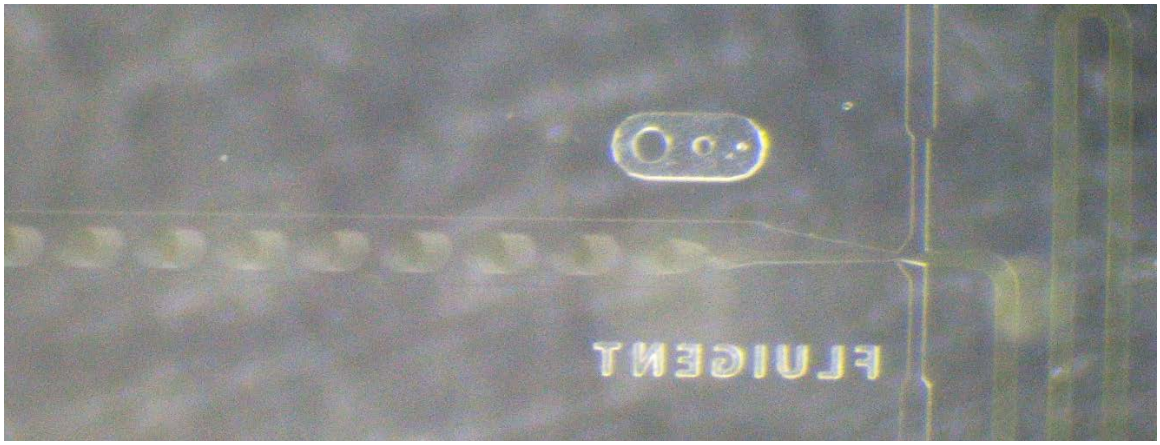

Figure 3-11: Particles in microfluidic channel.

For these experiments, two different types of continuous phase fluids were used. The first type is a mineral oil with no surfactant, and the second type is a mineral oil with surfactant

(commercial name span-80) at 2% volumetric ratio (v/v). The span-80 was expected to decrease the surface tension between oil and mixture polymer and dye. In addition, two different experiments were conducted. In the first, the dispersed phase (Polymer/dye mixture) was set at a fixed pressure; then the continuous phase (oil) pressure was increased from 1666.9 mbar to 1996.9 mbar. In the second experiment, the pressure of the mineral oil was fixed at a selected value while the pressure of the polymer/dye mixture was increased.

After each experiment, the chip was flushed with 91% isopropyl alcohol for approximately 30 min. In addition, the 1/16 inch outer diameter tubing, which is connected to the flow sensor of the aqueous phase pump much be changed every time in order to prevent contamination of working fluids. This is due to the fact that the mixture may cure due to exposure to light. In addition, the PDMS chip had no surface coating which contributed to easily removing the polymer/mixture from the channels. Also, the tip of the tubing should be cleaned every time with 91% isopropyl alcohol in order to prevent dust particles from entering the channel inside droplet generator chip. In addition, the microfluidic chip must be in a clean room or in closed container in order to prevent contamination with air particles [59]. In order to prevent this, a custom chip holder was fabricated in order to safely secure the chip. The details are shown in Appendix B.

To estimate the particle size, two methods are used: 1) by direct measurement of the particle employing the ruler that comes with the chip, and 2) the MATLAB's "imtool" image processing tool optimizes the image for post processing applications such as estimating dimensions. For the method 1), the particle is measured by directly comparing its size with the on board ruler. This ruler has 3 sizes which are 100 microns, 50 microns, and 20 microns

respectively. Figure 3-12 shows the ruler tool that was used to estimate the particles size in pixels. A reference was put at 100 microns diameter section.

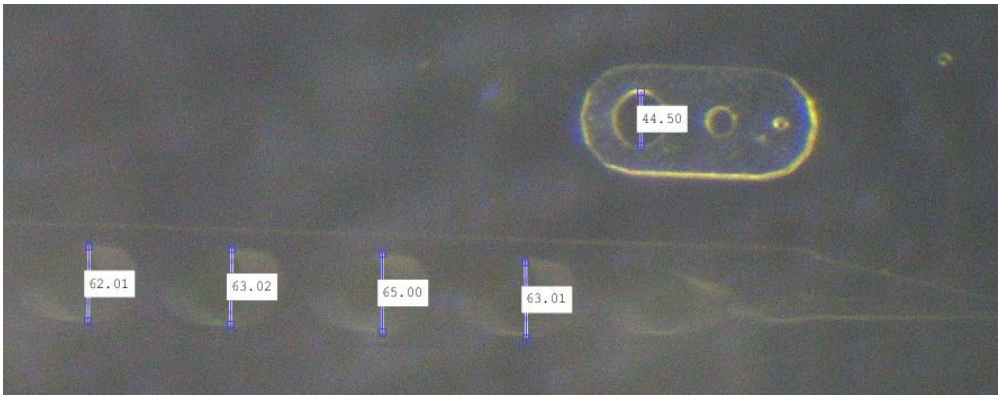

Figure 3-12: Diameter measurement (units in pixels).

A snapshot of every measurement was taken in order to estimate particles diameters at specified parameters. The microlasers diameters have been estimated by using photographs taken from a CMOS camera connected to a microscope. The photographs are then elaborated by using MATLAB image processing tool, which filters the image creating a better contrast of the particle's contour diameter to be measured. It has been found that a ~ 10% error is committed when the estimation of the microlaser's diameter is made without the MATLAB tool. Figure 3-13 shows a diameter reduction when the dispersed phase is fixed and continuous phase is increase. This is expected since the pinching of the dispersed phase by continuous phase is more efficient. In this case mineral oil was used the continuous phase and the polymer/dye of (4:1 PEGDA/Rhomadine-6g in ethanol 10^{-4}M). The top picture shows particles at ~151 micron and the bottom picture ~ 127 micron.

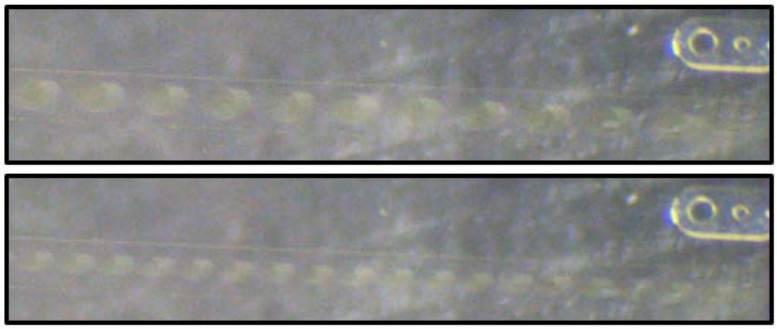

Figure 3-13: Images taken at fixed dispersed phase pressure of 479.9 mbar. Top: Mineral oil only at continuous phase pressure of 1666.9 mbar. Bottom: Mineral oil only at continuous phase pressure of 1996.9 mbar.

Conversely, figure 3-14 shows when case mineral oi with (2 % v/v) span-80 surfactant was used and continuous phase was fixed at 1666.9 mbar. The effects the increased dispersed phase was observed. It was expected the particle diameter should increase since a large blob of dispersed phase leads to larger diameter due to increase of dispersed phase pressure. Similarly, polymer/dye of (4:1 PEGDA/Rhomadine-6g in ethanol 10^{-4}M) was used as the dispersed phase. The top picture shows particles at ~97 micron and the bottom picture ~ 139 micron.

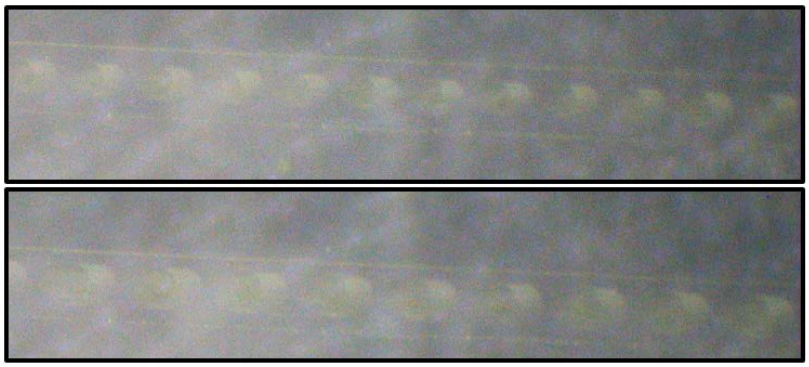

Figure 3-14: Images taken at fixed continuous phase pressure of 1666.9 mbar. Top: Mineral oil (2% v/v) Span-80 at dispersed phase pressure of 625 mbar. Bottom: Mineral oil (2%v/v) Span-80 at continuous phase pressure of 675 mbar.

Figure 3-15 shows a diameter reduction when the dispersed phase is fixed, and continuous phase is increase. This is expected since the pinching of the dispersed phase by

continuous phase is more efficient. In this case mineral oil with (2 % v/v) span-80 surfactant was used the continuous phase and the polymer/dye of (4:1 PEGDA/Rhomadine-6g in ethanol 10^{-4}M). The top picture shows particles at ~142 micron and the bottom picture ~ 86 micron.

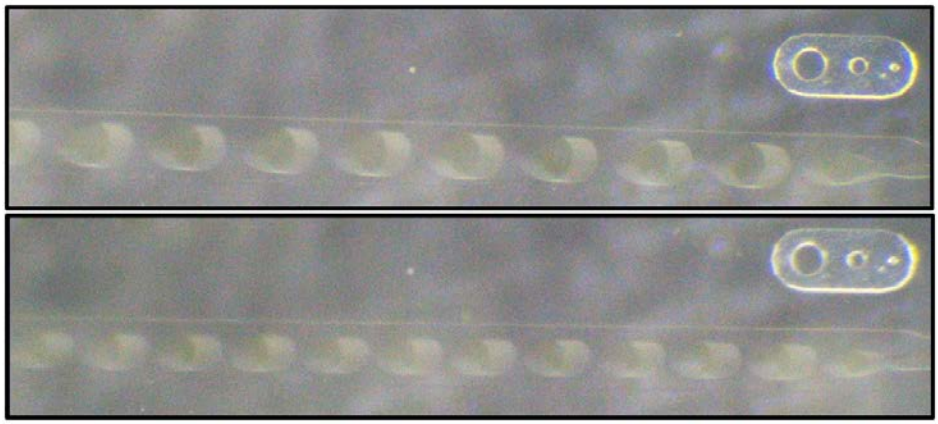

Figure 3-15: Images taken at fixed dispersed phase pressure of 570 mbar. Top: Mineral oil (2% v/v) Span-80 at continuous phase pressure of 1666.8 mbar. Bottom: Mineral oil (2%v/v) Span-80 at continuous phase pressure of 1996.9 mbar.

Therefore, it was found that an increase 14.3 mbar of continuous phase (mineral oil only) pressure decreases the particle diameter by 1 micron, while considering a fixed dispersed phase of (4:1 PEGDA/Rhomadine-6g in ethanol 10^{-4}M) pressure of 479.9 bar as shown in Figure 3-16.

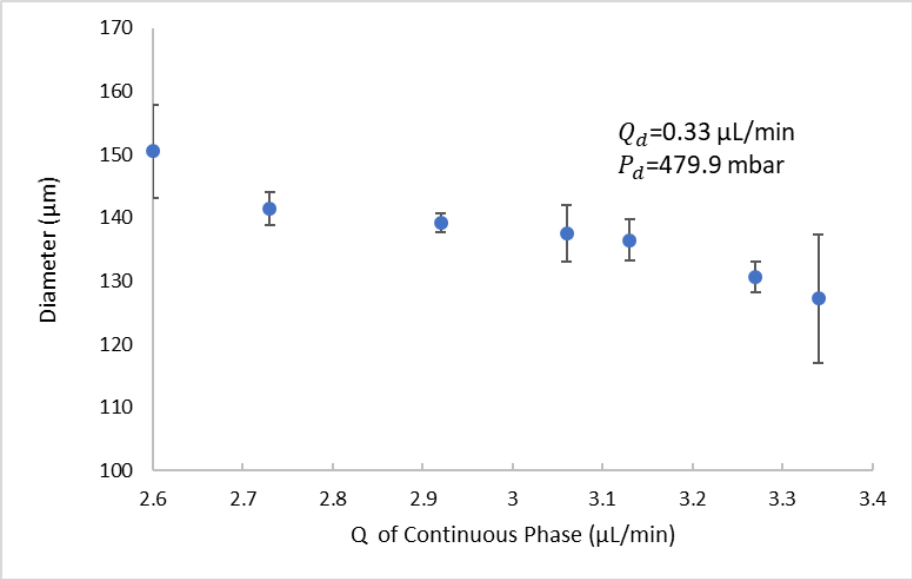

Figure 3-16: Mineral oil only at fixed dispersed phase flowrate of 0.33 µL/min.

Similarly, it was found that an increase of ~0.03 µL/min of continuous phase (mineral oil only) flowrate decreases the particle diameter by 1 micron, while considering a fixed dispersed of (4:1 PEGDA/Rhomadine-6g in ethanol 10^{-4}M) phase flowrate of 0.33 µL/min as shown in Figure 3-17.

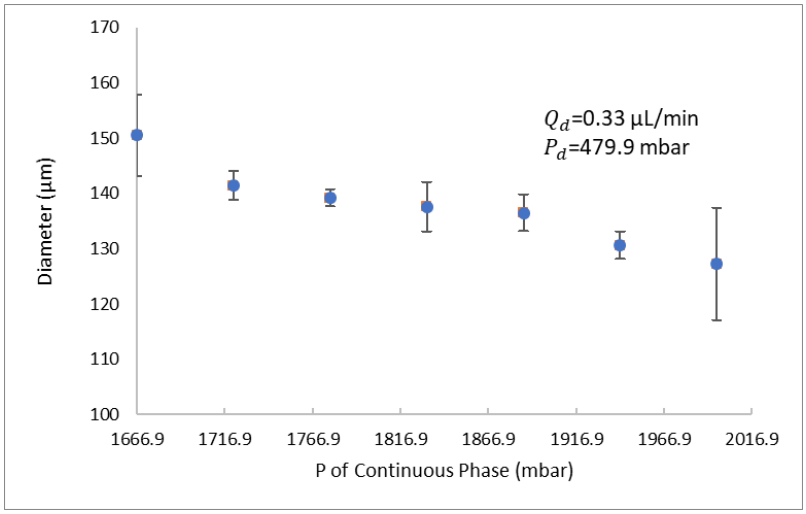

Figure 3-17: Mineral oil only at fixed dispersed phase pressure of 479.9 mbar.

However in Figure 3-18 it was found that an increase of ~0.006 µL/min of dispersed phase (4:1 PEGDA/Rhomadine-6g in ethanol 10^{-4}M) flowrate increases the particle diameter by 1 micron, while considering a fixed continuous phase (mineral oil) flowrate of 2.6 µL/min.

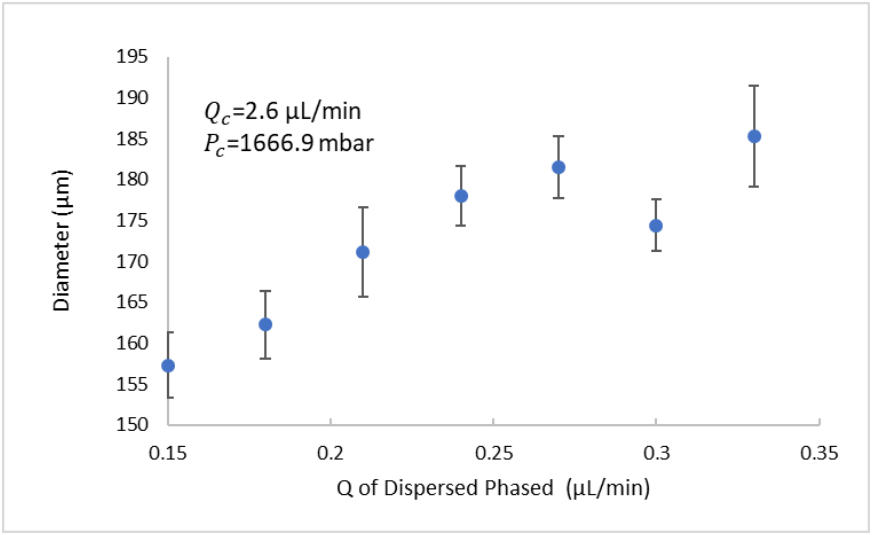

Figure 3-18: Mineral oil only at fixed continuous phase flowrate of 2.6 µL/min.

However, in Figure 3-19 it was found that an increase of ~2.1 mbar of dispersed phase (4:1 PEGDA/Rhomadine-6g in ethanol 10^{-4}M) pressure increases the particle diameter by 1 micron, while considering a fixed continuous phase (mineral oil) pressure of 1666.9 mbar.

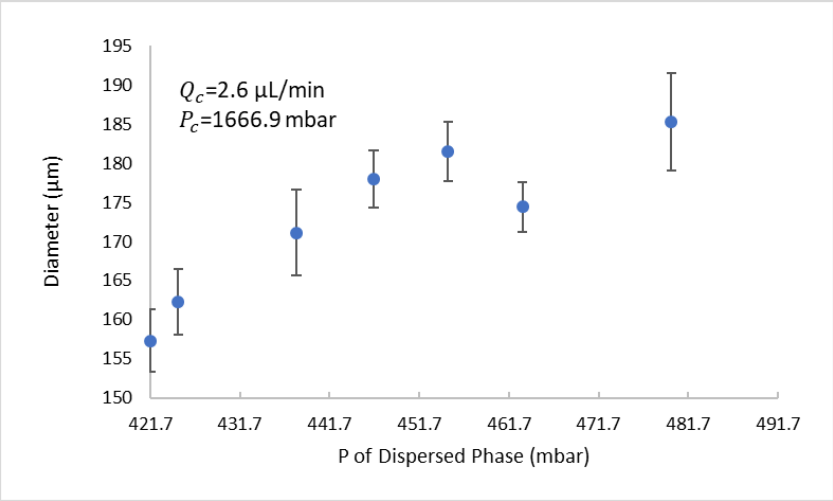

Figure 3-19: Mineral oil only at fixed continuous phase pressure of 1666.9 mbar.

Similarly, it was found that an increase of ~0.01 µL/min of continuous phase mineral oil with span-80 surfactant (2 % v/v) flowrate decreases the particle diameter by 1 micron, while considering a fixed dispersed phase of (4:1 PEGDA/Rhomadine-6g in ethanol 10^{-4}M) phase flowrate of 0.1 µL/min as shown in Figure 3-20.

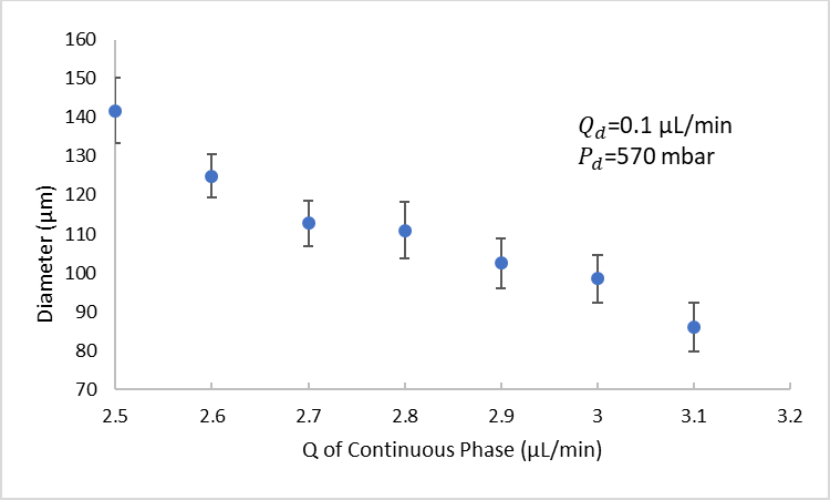

Figure 3-20: Mineral oil/Span-80 (2%v/v) at fixed dispersed phase flowrate of 0.1 µL/min.

Therefore, it was found that an increase of 5.93 mbar of continuous phase mineral oil with span-80 surfactant(2 v/v %) pressure decreases the particle diameter by 1 micron, while considering a fixed dispersed phase of (4:1 PEGDA/Rhomadine-6g in ethanol 10^{-4}M) pressure of 570 bar as shown in Figure 3-21.

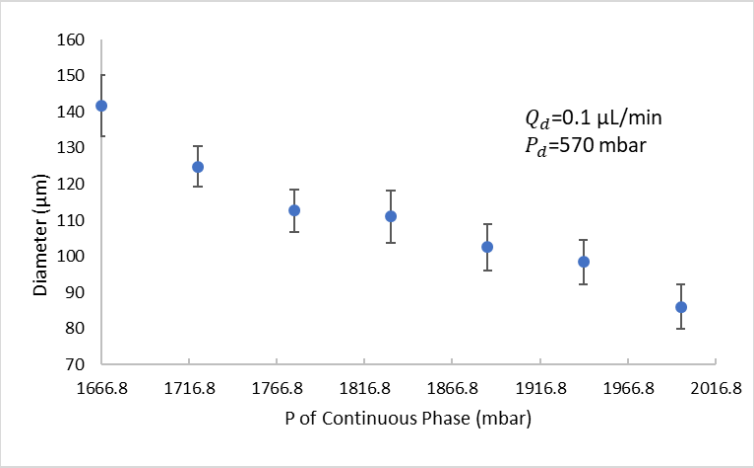

Figure 3-21: Mineral oil/Span-80 (2% v/v) at fixed dispersed phase pressure of 570 mbar.

However in Figure 3-22 it was found that an increase of ~1.2 mbar of dispersed phase (4:1 PEGDA/Rhomadine-6g in ethanol 10^{-4}M) pressure increases the particle diameter by 1 micron, while considering a fixed continuous phase mineral oil with span-80 surfactant (2% v/v) pressure of 1666.9 mbar.

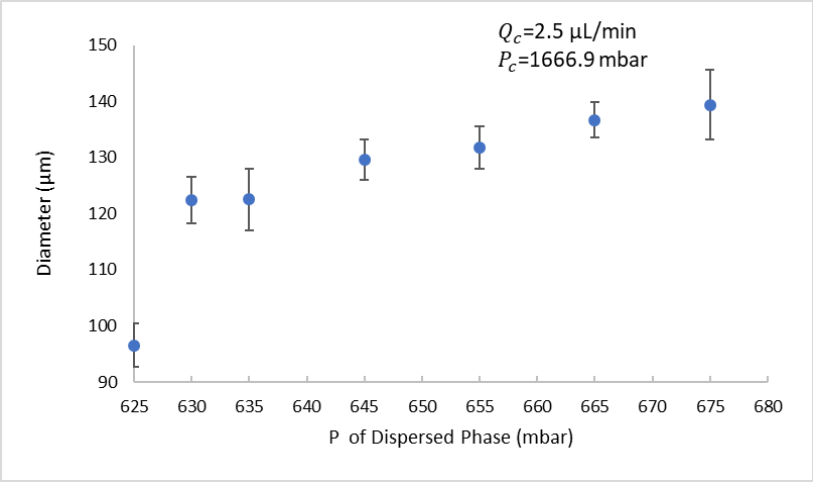

Figure 3-22: Mineral oil/Span-80 (2% v/v) at fixed continuous phase pressure of 1666.9 mbar.

Therefore, the results of these experiments establish the input parameters of flowrate and pressure needed to fabricate a microlaser of a certain size. It has been found that, the highest tunability of the microlaser's diameter is obtained by varying both the flow rate (Q) and the pressure (P) for the dispersed phase one at time (maintaining fixed all other parameters). Also, the diameter size is increasing with increasing Q and P values. Figure 3-23 shows the surface finish of fabricate particle. Overall, these results show that this fabrication method is suitable for making hydrophilic microlasers out of PEGDA or similar biocompatible hydrogels.

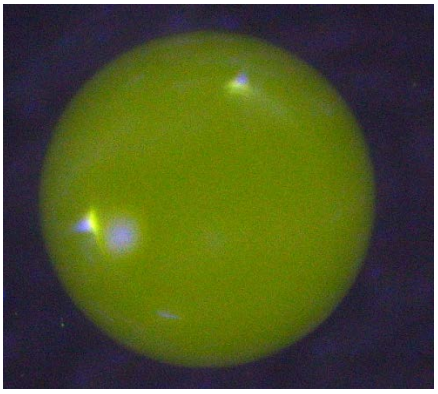

Figure 3-23: Particle fabricated by PDMS chip.

The particle was then placed on an optical fiber in order to allow for easier alignment to spectrometer. Figure 3-24 shows the results for emission spectra of a ~ 190 nm microlaser that was fabricated. Resonances are visible ~ between 573.5 nm - 576 nm. The emission spectra for microlaser fabricated by PDMS chip shows that the mineral oil does not affect the quality of the microlaser.

In fact, a quality factor of ~3.3* 10^4 was found. Also, the linewidth ($\delta\lambda$) was found to be ~0.0178 nm. This quality factor is similar to classical fabrication as reported by [14]. This confirms that the fabrication of polymeric microlasers by droplet generator method is successful. Therefore, this method can be implemented as a fast fabrication method of optical microlasers.

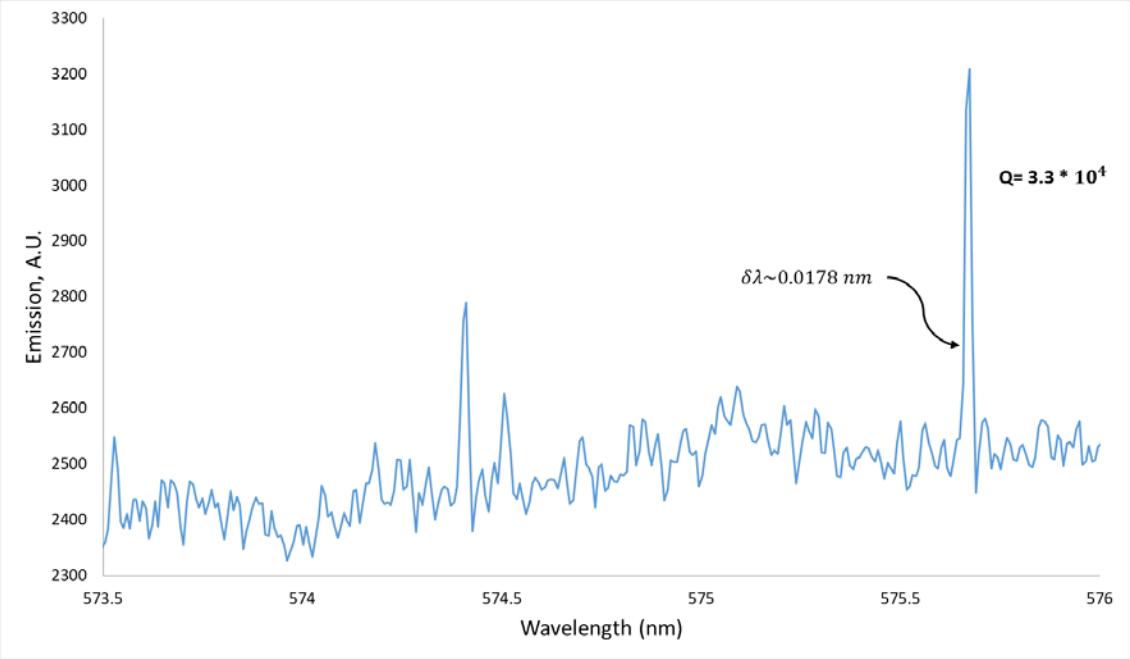

Figure 3-24: Spectra of microlaser fabricated by PDMS chip.

3.2.4 Glass Chip Method

3.2.4.1 Glass Chip Overview

The glass chip method consists of using a glass channel in order to make particles out of a hydrophobic polymer in a hydrophilic continuous phase. Figure 3-25 shows the glass chip and the focused flow junctions. The channel is 20 μm. The width of the chip is 2.55 cm, thickness of chip is 0.15 cm and the length 7.55 mm [60].

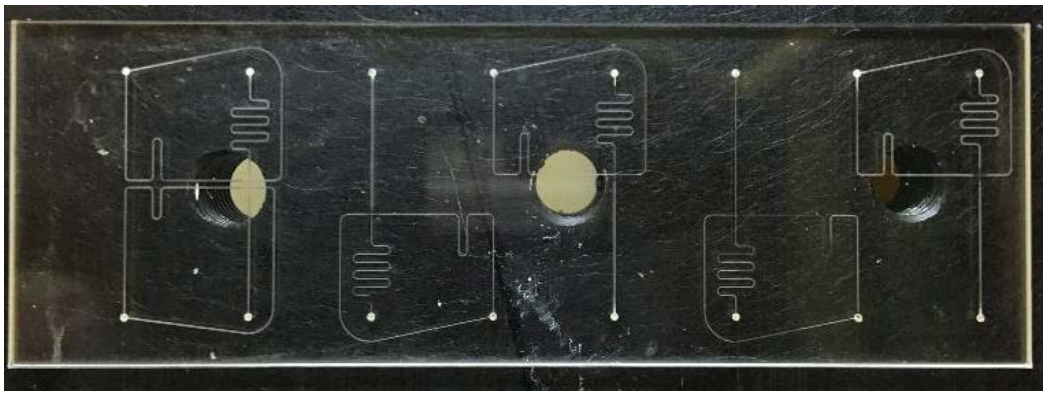

Figure 3-25: Glass chip.

The glass chip is connected to the microfluidic pumps by using a custom-made plate which allows to pushfit 2 mm outer diameter tubing to channel entrances. Applied pressure on top of plate allows a tight seal to be form between glass and tubing. Then 1/32 in outer diameter tubing is connected to the chip by using a sleeve made out of 0.5 mm outer diameter tubing. The outlet of the droplet generator is attached to reservoir, which holds freshly made particles. These 5 channels can be used to fabricate different hydrophobic polymer/dye mixtures at once. Therefore, this definite improvement of classical methods discussed.

3.2.4.2 Glass Chip Procedure and Scope

RBS-25 cleaning (2% v/v) in de-ionized water was used to clean glass material. This secures that the solution will not harm the sample and RBS-25 is known to clean laboratory glass ware [61]. Therefore, it is used to clean the glass chip for roughly 30 min after usage. The 1/16 inch outer tubing must be replaced every time that it used in order to avoid difficulties. Experimental results for glass chip is future work as indicated in Ch.5.

CHAPTER 4

PHOTONICS MICROLASERS IN BIOMEDICAL APPLICATIONS

4.1 Case Study 1: Electric Field Measurements via Resonator Doped with Di-Anepps-4 Voltage Sensitive Dye*

4.1.1 Motivation/Background for Voltage Sensitive Dye

Voltage sensitive dyes (VSDs) have optical properties such as absorption and fluorescence, which are sensitive to membrane potential. Therefore, they can be used to measure human brain activity at many locations [62]. According to previous studies, VSDs are being used at low concentrations to provide acceptable sensitivity and minimize possible side effects [63,64]. Optical methods, such as multiphoton microscopy, have been developed to investigate cellular physiological activity [65]. This method with fluorescence VSDs has successfully monitored transmembrane voltage changes of neurons [65]. Overall, VSDs will provide researchers with an effective method to measure the complex activity of neuron network and their membrane potential changes.

4.1.2 Experimental Setup

The spectroscopy setup is used to excite the optical laser modes of the dye-doped resonator. The microlaser is placed between two electrodes which are connected to a power supply. By varying the power supply's voltage is possible to change the electric field generated between the electrodes as shown in Figure 4-1 [66]. The particle was made with Norland Blocking Adhesive (NBA) and Di-4 Amino-Naphthyl-Ethylene-Pyridinium-Propyl-Sulfonate (ANEPPS)

* Section 4.1 is reproduced from M. Manzo and O. Cavazos, "Neurotransducers Based Voltage Sensitive Dye-Doped Microlasers," Optical Society of America :Biophotonics Congress (2019). Authors retain copyright.

voltage sensitive dye. The laser dye was dissolved in (95%) ethanol with concentration of 10^{-5} M in a polymer to dye ratio of (4 to 1).

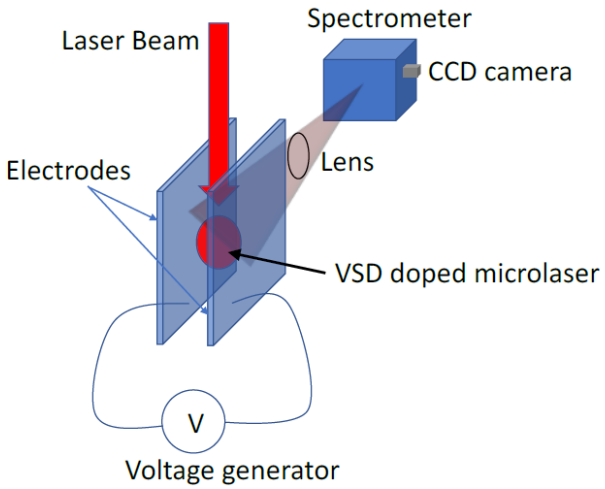

Figure 4-1: Electric field setup. [66]

4.1.3 Experimental Results and Discussions

Figure 4-2 shows a blue shift in the laser modes when the electric field is increased. As described previously only morphology change of the microlaser leads to a shift in the optical modes. Therefore, the microlaser is not deformed in anyway, only a refractive index change can lead to the shift. This VSD based microlaser can possibly be used for brain imaging applications.

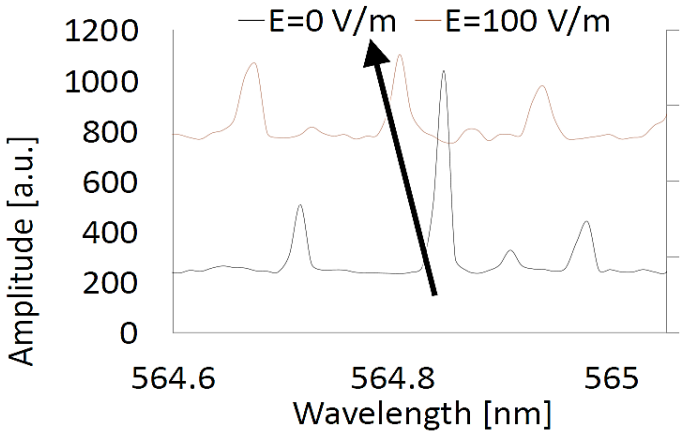

Figure 4-2: Spectra of 2 voltage values. [66]

Figure 4-3 shows the relationship between the optical modes shift and the electric field variation between the electrodes due to a change in the voltage. An almost linear relationship was found with a sensitivity of $\frac{\Delta\lambda}{\Delta E}$ = -0.0005 $\frac{nm}{\frac{V}{m}}$. The advantage of this concept is that the microlaser can sense a perturbation of the electric field without being embedded into the cellular membrane.

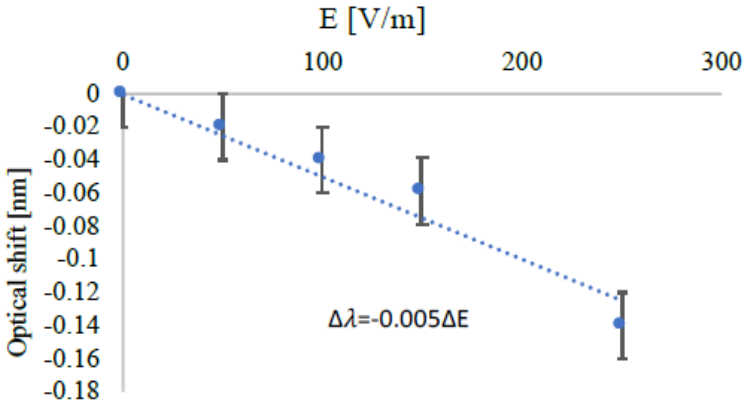

Figure 4-3: Linear relationship between optical shift and electric field variation. [66]

4.2 Case Study 2: Strain Measurements in a 3D Printed Bone-Like Structure to Mimic Biomedical Implantable Sensors*

4.2.1 Motivation for Bone Testing

Biomechanics is essential for developing medical devices for human bones [67]. The strain and stress of human are critical to design proper implants and to heal bone tissues due to stability and mechanical strength [68]. Traumatologists frequently use conventional imaging systems to monitor bone healing, but sometimes it is not accessible due to the material of the implant [69]. For these reasons, embedded microsensors can improve the monitoring process. Several types

* Section 4.2 is reproduced from O. Cavazos, M. Manzo, H. R. Siller, and E. Ramírez-Cedillo,"Bone-Integrated Optical Microlasers for in-vivo Diagnostic Biomechanical Performances," ASME International Mechanical Engineering Congress and Exposition 2019 (accepted); with permission from ASME.

biosensors have been developed such as wired gages [70], biomedical microelectromechanical systems (bioMEMS) [71], whispering gallery mode [72-75]and fiber optic sensors (FOS) [76-79].

When implants are integrated with bones after surgery, osseointegration can compromise the structural integrity of bones. Therefore it is important to monitor mechanical properties of bones by in-vivo monitoring. In this case study, it is proposed to integrate optical microlasers into bones.

4.2.2 Experimental Setup

To simulate the working principle, a sensor is integrated was integrated with the 3-D printed bone [4]. The photonic microlasers are fabricated by using a liquid polymer mixture made of polyethylene (glycol) diacrylate PEGDA-700 and thiocure trimethylolpropane tri (3-mercaptopropionate) TMPMP (4:1 by volume). Thiocure TMPMP was implemented in order to make softer particles [4]. Then a solution of rhodamine 6g laser dye was dissolved in 95% ethanol (Sigma-Aldrich) with a concentration of ~10^{-4} M. Therefore, a polymer- dye mixture in volume with 4 parts of polymers solution and one part of dye solution. After that, the particles were placed near the top center surface of the cortical bone-like as shown in Figure 4-4.

The particle was placed in the center of the bone at top surface, which allows for the local strain experienced by bone in the cantilever end load configuration to be experienced by the particle. The optical post assembly (cantilever support) was mounted on a translation stage in order to allow for alignment of the particle. Therefore, the mechanical setup is movable and can be aligned with monitoring setup efficiently. The optical setup used is showed in Figure 4-4 and is similar to the one described in Chapter 2.

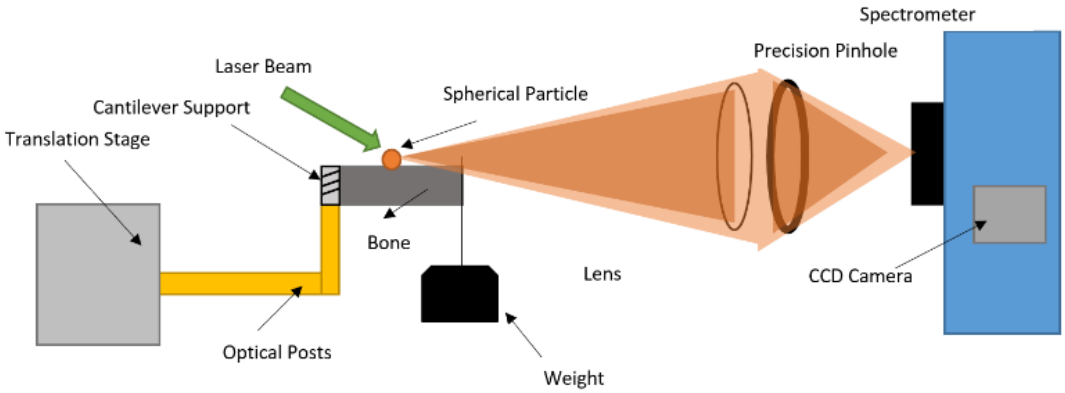

Figure 4-4: Biomechanical setup. [4]

The particle that was used for this experiment was ~ 616 microns. The experiment was done for 3 different loads of 0.10 kg, 0.070 kg, 0.050 kg as shown with setup in Chapter 2.

4.2.3 Mathematical Model

A mathematical model was used in order to determine local strain at the photonic sensor's location. A cantilever beam with an end load is assumed. Equation (21) shows an equation derived from Hooke's law. Here M is moment experienced at the location of interest. C is the distance from center of the beam. I is the moment of inertia of the bone. E is the modulus of elasticity [80].

$$\epsilon = \frac{Mc}{IE} \tag{21}$$

Equation (22) was used to find the moment at the local of the surface. Therefore, the top surface of the beam was referenced when solving for strain.

$$M = F(X - L) \tag{22}$$

The microlaser is shown on the beam in Figure 4-5.

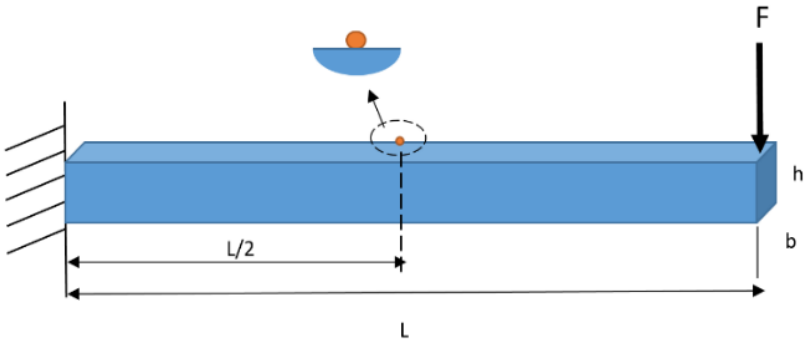

Figure 4-5: Beam schematic. [4]

4.2.4 Experimental Results and Discussions

A conservative estimate of local strain applied the microlaser can be estimated by equation (3), which was discussed previously. Table 4-1 shows the results of the analysis.

Table 4.1: Results of Analysis [4]

Mass (kg)	Force (N)	Tensile Strain (m/m)	Bone Stress (Pa)	Particle Stress (Pa)
0.05	0.4905	0.0000587	104,000	0.61
0.07	0.6867	0.0000821	145,500	0.85
0.10	0.981	0.0001173	207,900	1.22

The resonance wavelength used for evaluating the strain was selected to be ~ 570.43 nm, with a linewidth of ~0.01068 nm. Therefore, the strain of the particle can be estimate from the shift of this resonance as shown in Equation (23).

$$\varepsilon = \frac{\Delta R}{R} \sim \frac{\Delta \lambda}{\lambda} \tag{23}$$

Then it was assumed that the particle strain should be similar to the bone strain as shown in Table 4-2.

Table 4.2: Strain Comparison [4]

Force (N)	Particle Strain ~ $(\frac{\Delta\lambda}{\lambda})$	Bone Strain $(\frac{\sigma}{E})$	Relative Error
0.4905	0.000024	0.0000587	1.5
0.6867	0.000105937	0.0000821	0.23
0.981	0.00012359	0.0001173	0.05

After conducting the experiment, a negative optical shift was discovered due to the tensile strain on the top surface of the bone. Figure 4-6 shows a linear relationship optical shift change and change in local strain. A linear regression was performed in order to determine the sensitivity, which was deemed to be ~0.0006 $\frac{nm}{\mu\varepsilon}$.

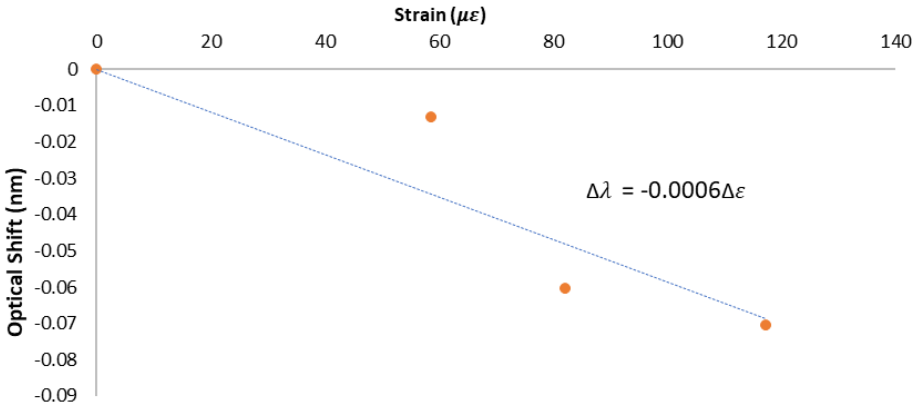

Figure 4-6: Linear relationship between strain and optical shift. [4]

It is observed that optical resonances did experience a "blue" shift. Also, it shown that the amplitude was slightly increased. Figure 4-7 shows the data for the load scenario of 0.69 N (0.07 kg).

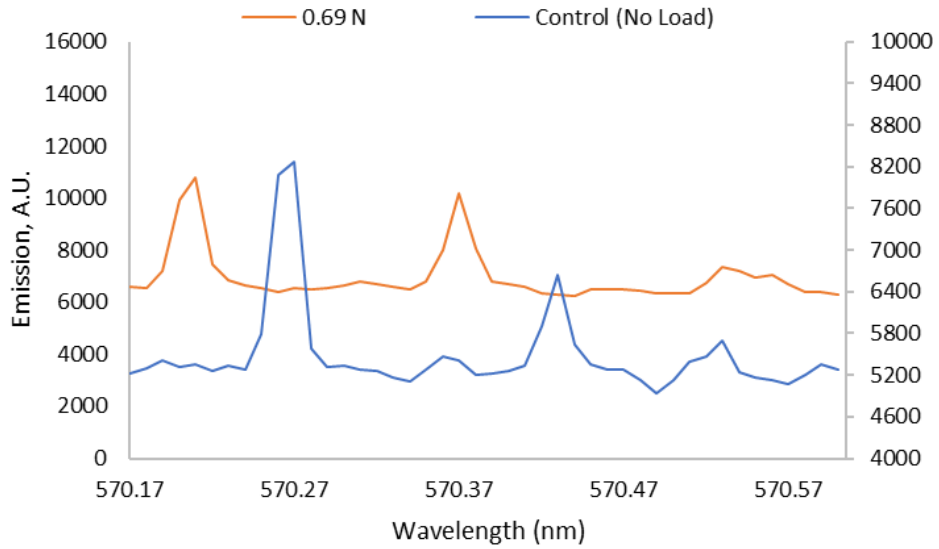

Figure 4-7: Blue shift of spectra for 0.69 N load. [4]

The resolution of sensor can be found by simply using a conservative approach shown in Equation (23) [8].

$$\delta_{\varepsilon} = \frac{\lambda}{Q}\left(\frac{d\lambda}{d\varepsilon}\right)^{-1} \tag{23}$$

A “blue shift” of the optical modes was witnessed. Also, a resolution of ~ 0.000018 $\frac{m}{m}$ and a quality factor of 5.34 * 10^4 were reported. Therefore, one possible application of this technology is that it can be used to monitor patients with osteoporosis.

CHAPTER 5

CONCLUSION AND FUTURE WORK

In this thesis, a new fabrication method based microfluidic lab-on-a-chip for fabricating optical microlasers is presented and demonstrated. The proposed technique aims to substitute current methods for the mass production of microlasers. The experiments carried out in chapter 3 shows two parameters are of importance for the fabrication of microlasers with a preselected size: the flow rate (Q) and the pressure (P) values for the dispersed and continuous phases. The microfluidic chip channel used is Chapter 3. It has been found that, the highest tunability of the microlaser's diameter is obtained by varying both the flow rate Q and the pressure P for the dispersed phase one at time (maintaining fixed all other parameters). Also, the diameter size is increasing with increasing Q and P values. On the other hand, by varying the flow rate Q and pressure P of the continuous phase one at time (maintaining fixed Q and P for the dispersed phase) is possible to obtain microlasers with smaller sizes (the diameter is decreasing with increasing Q and P values), which result in a lower tunability of the microlaser's size. The microlasers diameters have been estimated by using photographs taken from a CMOS camera connected to a microscope. Finally, the microlasers fabricated exhibited a quality factor Q of ~ $3.3* 10^4$, which is comparable with Q from microlasers made with other methods. In chapter 4, the microlaser is made by using a voltage sensitive dye named DI-4-ANNEPS. The experimental results showed measurements of the electric field between 0 and 250 V/m and the optical shift was found to be negative due to a negative variation of the refractive index of the VSD with the increment of voltage. A nearly linear behavior was found between the electric field variation and the optical shift. The sensitivity and resolution were found to be $\Delta\lambda/\Delta E=-5*10^{-4}$ nm/(V/m) and 34

V/m, respectively. This can be used as optical neurotransducer and can detect nerve cells' electrical activities by the perturbation of the evanescent field with a high sensitivity and resolution. In addition, microlasers are also demonstrated to be used for measurements of strain, when implanted in bones. The sensor is embedded in a 3-D printed bone. A mathematical model is correlated with the optical shift of the laser modes of the microlaser used. It is found that a "blue shift" of the laser modes is present with the increased strain. In addition, a resolution of ~ 0.000018 and a sensitivity of -0.000018 $\frac{m}{m}$ were found. This sensor can be used to test more cortical bone-like samples and attempt to provide fundamental contributions to the biomechanical testing of implants. Future studies will include test different materials for fabricating microlasers. In addition, the use of other types of microchips will be explored, such as silica droplet generator chip.

APPENDIX A

DESIGN DRAWINGS FOR FLUID RESERVOIR STAND

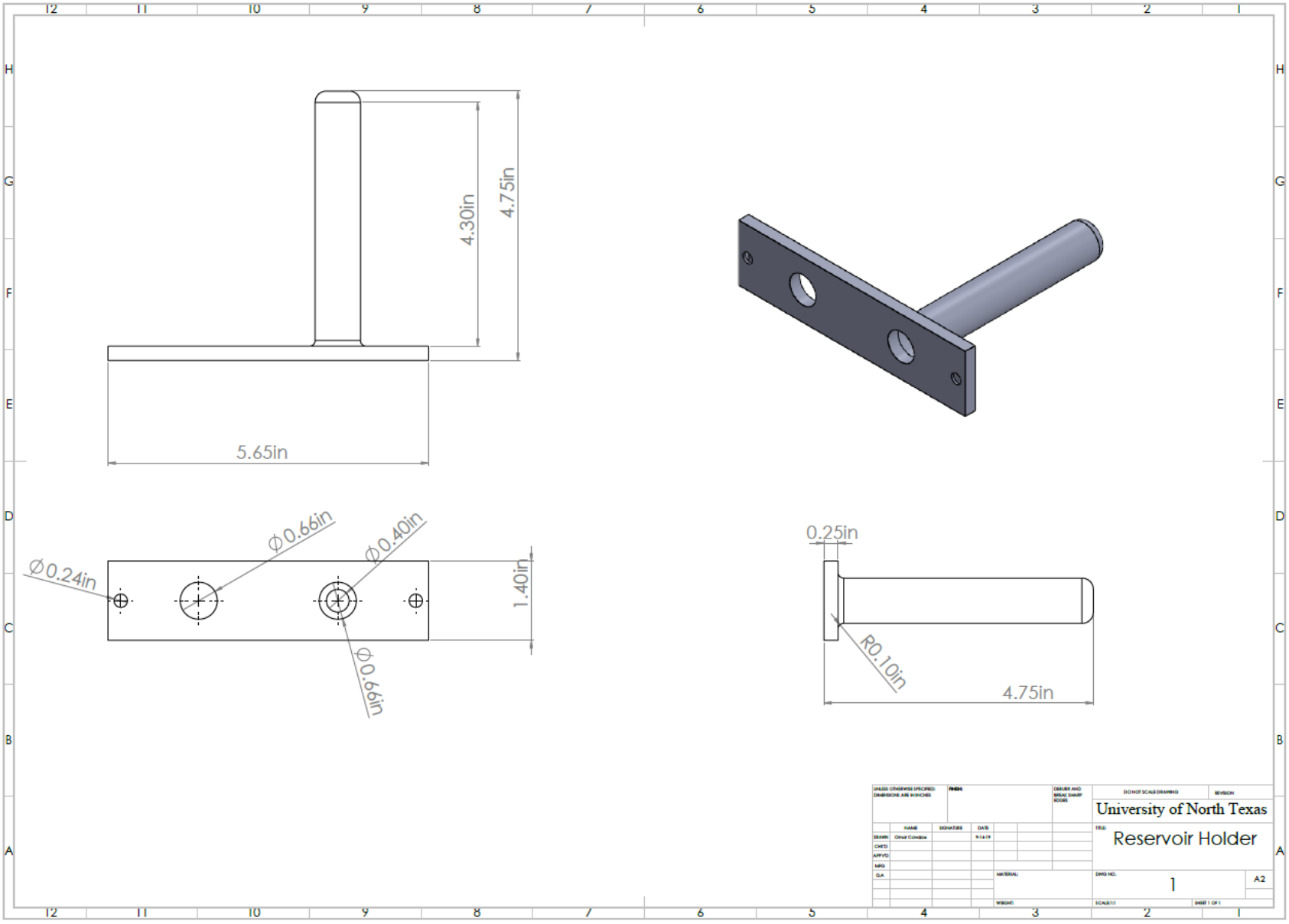
4.30in
4.75in
5.65in
Ø0.66in
Ø0.40in
Ø0.24in
1.40in
Ø0.69in
0.25in
R0.10in
4.75in
University of North Texas
Reservoir Holder
1
A2

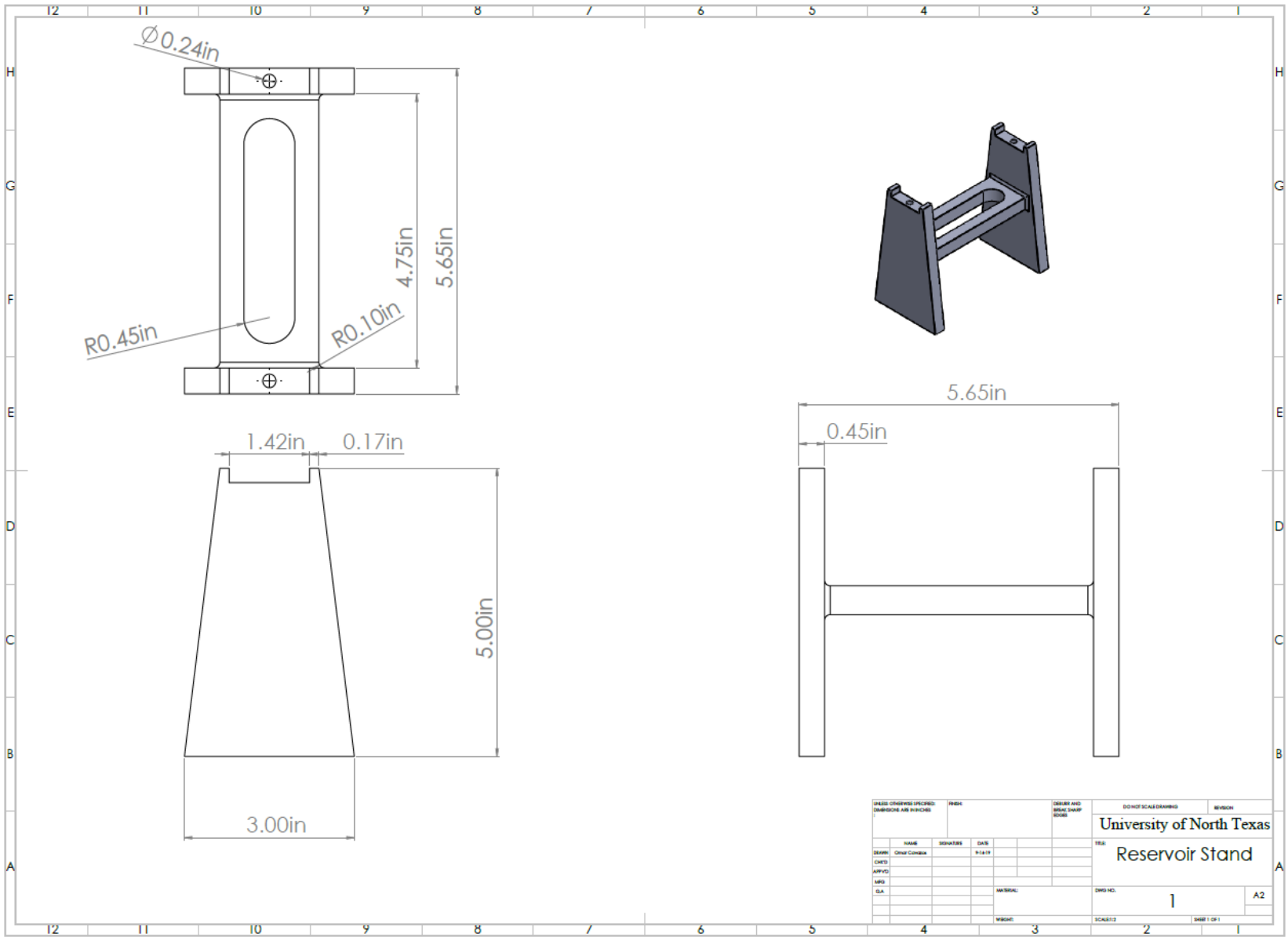
Ø0.24in
4.75in
5.65in
R0.45in
R0.10in
1.42in
0.17in
5.00in
3.00in
5.65in
0.45in
University of North Texas
Reservoir Stand
1
A2

APPENDIX B

DESIGN DRAWINGS FOR MICROFLUIDIC CHIP HOLDER

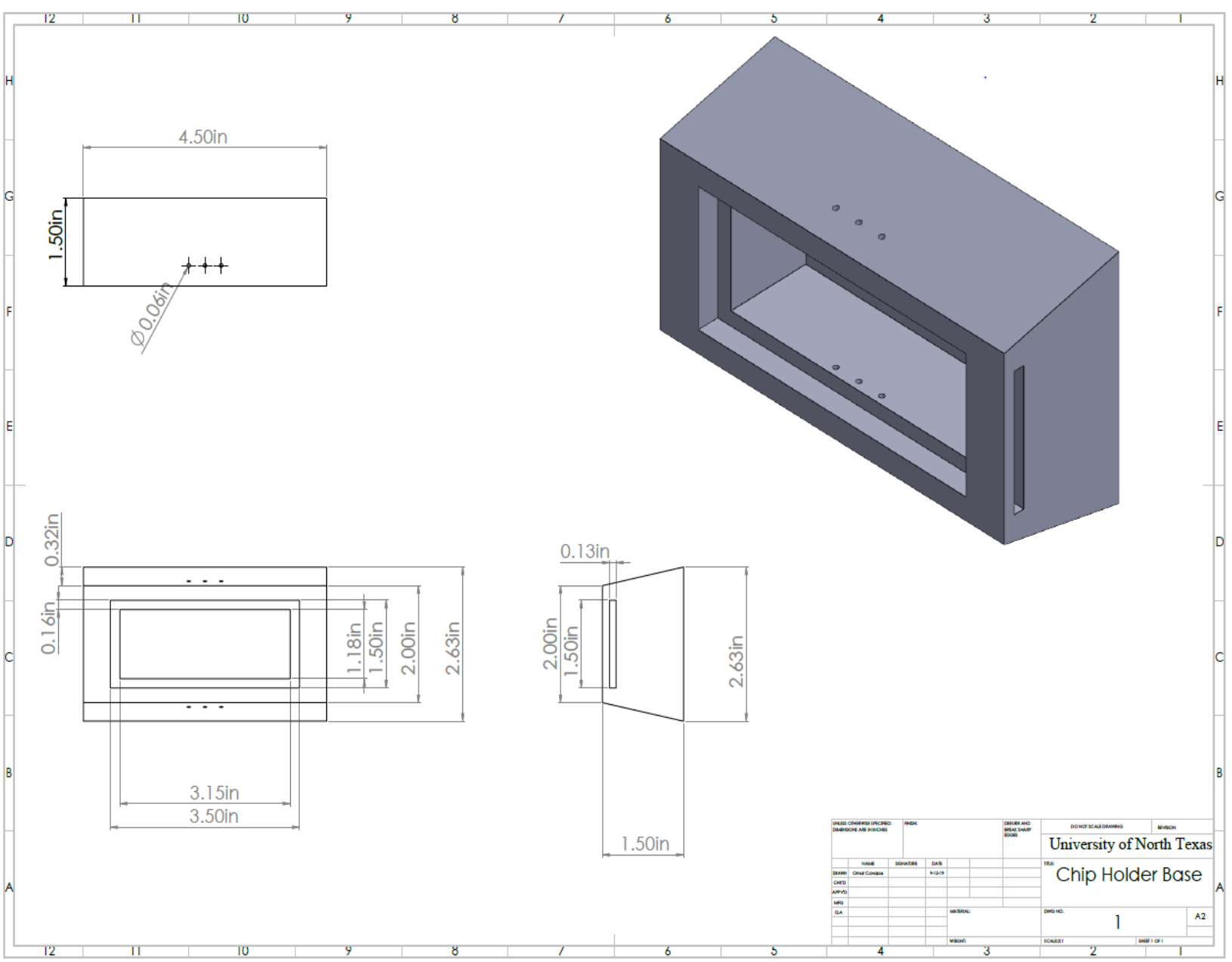
4.50in
1.50in
Ø0.06in
0.32in
0.16in
1.18in
1.50in
2.00in
2.63in
3.15in
3.50in
0.13in
2.00in
1.50in
2.63in
1.50in
University of North Texas
Chip Holder Base
1
A2

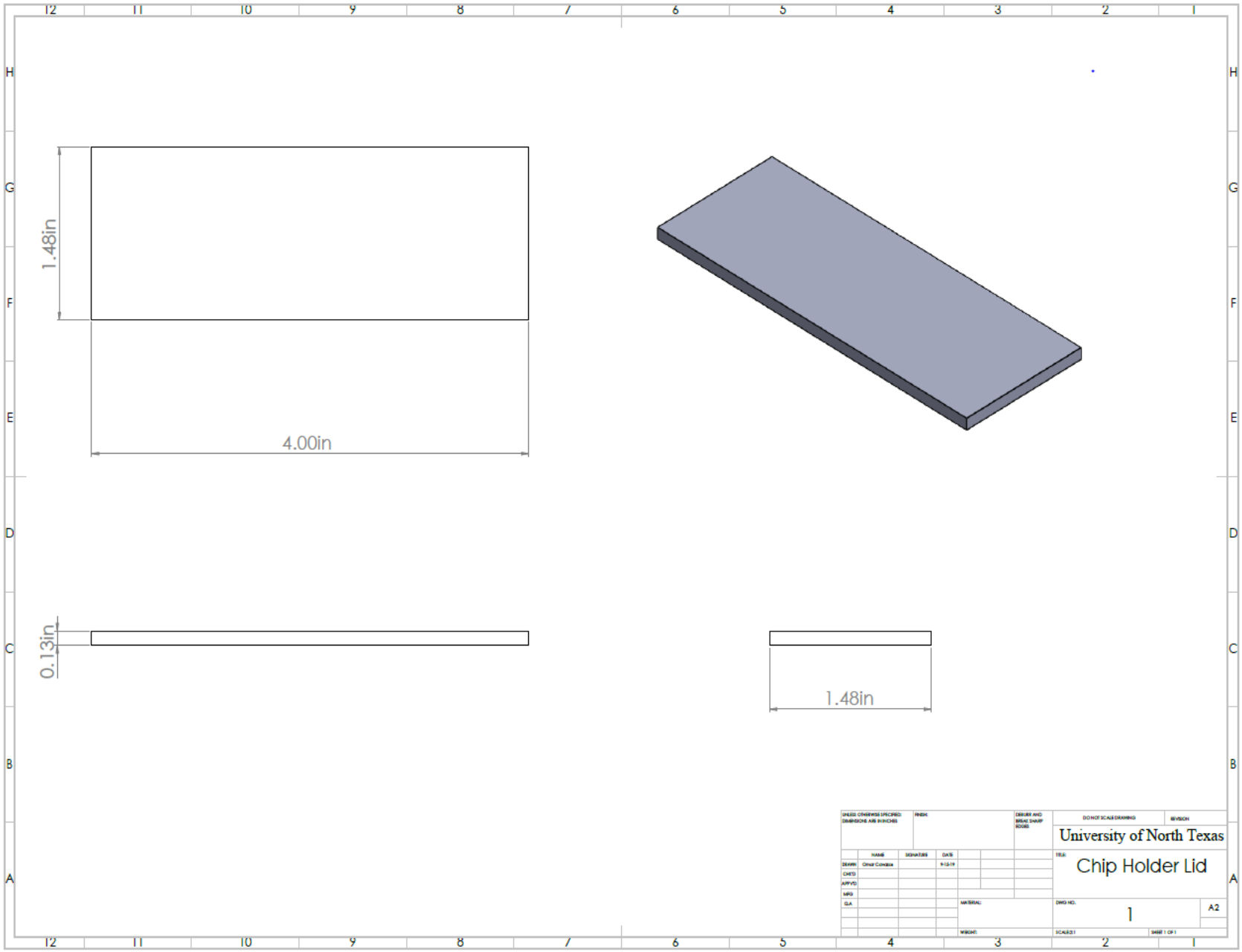
1.48in
4.00in
0.13in
1.48in
University of North Texas
Chip Holder Lid
1
A2

REFERENCES

1. B. Luo, S. Wu, Z. Zhang, W. Zou, S. Shi, M. Zhao, N. Zhong, Y. Liu, X. Zou, L. Wang, el at, Human heart failure biomarker immunosensor based on excessively tilted fiber gratings, Biomedical Optics Express, 8 *(*2017), 57-67.

2. J. Liang, C. Yao, X. Li, Z. Wu, C. Huang, Q. Fu, C. Lan, D. Cao, and Y. Tang, Silver nanoprism etching-based plasmonic ELISA for the high sensitive detective of prostate-specific antigen. Biosensors and Bioelectronics 69 (2015), 128-134.

3. L. Zhang, Y. Zhang, Y. Hu, Q. Fan, W. Yang, A. Li, S. Li, W. Huang, L. Wang, Refractive index dependent real-time plasmonic nanoprobes on a single nanocube for ultrasensitive detection of lung cancer-associated miRNAs, Chemical Communications, 15 (2015) 294-297.

4. O. Cavazos, M. Manzo, H. R. Siller, and E. Ramírez-Cedillo,"Bone-integrated optical microlasers for in-vivo diagnostic biomechanical performances", ASME International Mechanical Engineering Congress and Exposition 2019 (accepted).

5. https://www.elprocus.com/optical-sensors-types-basics-and-applications/

6. https://lasers.llnl.gov/education/how_lasers_work

7. B.E.A. Saleh and M. C. Teich, "Fundamentals of Photonics", John Wiley and Sons Inc (2007).

8. http://legacy.jyi.org/volumes/volume3/issue3/fetures/peterson.html

9. https://www.rp-photonics.com/gain_media.html

10. https://www.rp-photonics.com/four_level_and_three_level_gain_media.html

11. https://www.americanscientist.org/sites/americanscientist.org/files/201085162648063-2010-09DitmireF2.jpg

12. https://www.rp-photonics.com/laser_transitions.html

13. H. Haken, 1970, "Laser Theory," Light and Matter Ic. Encyclopedia of Physics, vol 5 / 25 / 2 / 2c.

14. M. Manzo, R. Schwend, A Novel Microlaser based Plasmonic-Polymer Hybrid Resonator for Multiplexed Bio-sensing, ASME Journal. of Medical Diagnostics, 4 (2018).

15. https://www.photonics.com/images/Web/Articles/2010/12/14/thumbnail_45296.dome.jpg

16. M. Manzo, O. Cavazos, “A wireless photonic intraocular pressure sensor”, ASME IMECE 17.

17. Manzo, M., Ioppolo, T., LaPenna, V., Ayaz, U., and Otugen, V. “A photonic wall pressure sensor for fluid mechanics applications.”, Rev. Sci. Instrum 83 (2012).

18. L. Zhao, Y. Wang, Y. Yuan, Y. Liu, S. Liu, W. Sun, J. Yang, and H. Li, Whispering gallery mode laser based on cholesteric liquid crystal microdroplets as temperature sensor, Optics Communications 402 (2017) 181-185.

19. Q.-L. Huang, H.-L. Xu, M.-T. Li, Z.-S. Hou, C. Lv, X-P. Zhan, H.-L. Li, H. Xia, H.-Y. Wang, H.-B. Sun, Stretchable PEG-DA Hydrogel-Based Whispering-Gallery-Mode Microlaser with Humidity Responsiveness, Journal of Lightwave Technology 36 (2018) 819-824.

20. B. $\ddot{O}$zel, R. Nett, T. Weigel, G. Schweiger, A. Ostendorf, Temperature sensing by using whispering gallery modes with hollow core fibers, Measurement Science and Technology 21 (2010).

21. Z.-P. Liu, Y. Li, Y.-F. Xiao, B.- B. Li, X.-F. Jiang, Y. Qin, X.-B. Feng, H. Yang, and Q. Gong, Direct laser writing of whispering gallery microcavities by two-photon polymerization, Applied Physics Letters, 97 (2010).

22. D. Zhang, L. Men, and Q. Chen, Femtosecond laser fabricated polymer microring resonator for sensing applications, Electronics Letters, 54 (2018) 888-890.

23. L. Wu, Z. Shen, Y. Zheng, Z. Cai, and X. Chen, Whispering gallery mode microlaser based on a fiber-stand polydimethylsiloxane microresonator, Optical Engineering 53 (2014).

24. S.K. Vanga, and A.A. Bettiol, Proton beam writing of dye doped polymer microlasers, Nuclear Instruments and methods in physics research B. 348 (2015) 209-212.

25. S.K. Vanga, and A.A. Bettiol, Proton beam writing of three-dimensional microcavities, Nuclear Instruments and methods in physics research B. 306 (2013) 281-283.

26. S.K. Vanga, V. Nalla, and A.A. Bettiol, Polymer microlasers with a suspended cavity design, Optical Materials. 42 (2015) 144-147.

27. N.B. Tomazio, L. De Boni, and C.R. Mendonca, Low threshold rhodmanine-doped whispering gallery mode microlasers fabricated by direct laser writing, Scientific Reports. 7 (2017).

28. A. Madani, H. Azarinia, and H. Latifi, Design and fabrication of polymer micro ring resonator with novel optical material at add/drop geometry using laser beam direct write lithography, Optik. 124 (2013) 1746-1748.

29. R. Kirchner, A. Finn, R. Landgraf, L. Nueske, L. Teng, M. Vogle, and W.-J. Fischer, Direct UV-Imprinting of Hybrid-Polymer Photonic Microring Resonators and Their Characterization, Journal of Lightwave Technology. 32 (2014).

30. U. Levy, K. Campbell, A. Groisman, S. Mookherjea and Yeshaiahu Fainman, On-chip microfluidic tuning of an optical microring resonator, Applied Physics Letter 88 (2006).

31. C. Monat, P. Domachuk, and B.J. Eggleton, Integrated Optofluidics: A new river of light, nature photonics. 1 (2007).

32. Z. Li, and D. Psaltis, Optofluidic dye lasers, Microfluid Nanofluid. 4 (2008) 145-158.

33. K. Gardner, M. Aghajamali, S. Vagin, J. Pille, W. Morrish, J.G.C. Veinot, B. Rieger, and A. Meldrum, Ultrabright Fluorescent and Lasing Microspheres from a conjugated polymer, Advanced Functional Materials. 28 (2018).

34. G. Aubry, C. Wang, J. Soto-Velasco, S. Méance, A.-M. Haghri-Gosnet, Q. Kou, On-chip production of liquid optical microcavities, Microelectronic Engineering 88 (2011) 2618-2621.

35. T. Nisisako, T. Torii, and T. Higuchi, Novel micro reactors for functional polymer beads, Chemical Engineering Journal. 101 (2004) 23-29.

36. S. Anand, M. Ery$\ddot{u}$rek, Y. Karadag, A. Erten, A. Serpeng$\ddot{u}$zel, A. Jon$\acute{a}\check{s}$, A. Kiraz, Observation of whispering gallery modes in elastic light scattering from microdroplets optically trapped in a microfluidic channel, Journal of the Optical society of America B, 33 (2016).

37. H. A. Stone, S. Kim, Microfluidics: Basic issues, Application, and Challenges, American Institute of Chemical Engineers Journal, 47 (2001).

38. G. Aubry, M. Zhan, H. Lu, Hydrogel-droplet microfluidic platform for high-resolution imaging and sorting of early larval Caenorhabditis elegans, Lab Chip 15 (2015) 1424-1431.

39. S. Mashaghi , A. Abbaspourrad, D.A. Weitz, A.M. van Oijen, Droplet microfluidics: A tool for biology, chemistry, and nanotechnology, Trends in Analytical Chemistry 82 (2016) 118-125.

40. S.-Y. Teh, R. Lin, L.-H. Hung, and A. P. Lee, Droplet microfluidics, Lab Chip, 8 (2008) 198 - 220.

41. https://www.mcphersoninc.com/spectrometers/uvvisir/model209.html

42. https://www.newport.com/t/getting-light-into-a-monochromator

43. https://www.fluigent.com/product/microfluidic-components/lineup-series/#specifications

44. https://www.fluigent.com/product/microfluidic-components/reservoirs-p-cap/#1529003923486-cc0105d2-f131b162-40deefb1-9ac429c0-df3904dd-bfcc

45. C. Kleinstreuer, Microfluidics and Nanofluidics: Theory and Selected Applictations, John Wiley & Sons Inc., Hoboken, NJ, 2013

46. J. Berthier and Silberzan, Microfluidics for Biotechnology, Artech House, 2009.

47. P. Tabeling, and S. Cheng, Introduction to Microfluidics, Oxford University Press, 2006.

48. N.-T. Nguyen, and S. T. Wereley, Fundamentals and Applications of Microfluidics, Artech House, 2006.

49. S. Prakash, and J. Yeom, Nanofluidics and Microfluidics, Waltham: William Andrew (2014).

50. C.T. Crowe, J. D. Schwarzkopf, M. Sommerfeld, and Y. Tsuji, Multiphase Flows with Droplets and Particles, Taylor and Francis Group (2012).

51. E.E. Michaelides, Particles, Bubbles and Drops : Their Motion, Heat and Mass Transfer, World Scientific Co Pte Ltd, 2006.

52. R.W. Fox, P. J. Pritchard, and A.T. McDonald, Introduction to Fluid Mechanics, John Wiley & Sons Inc., Hoboken, NJ, 2009.

53. F. M. White, Fluid Mechanics, McGraw-Hill, New York, NY, 2001.

54. X. C. I. Solvas, and A. DeMello, Droplet microfluidics: recent developments and future applications. Chemical Communications, 47 (2011)1936-1942.

55. J.-C. Baret, Surfactants in droplet-based microfluidics, Lab Chip, 12 (2012) 422-433.

56. https://www.nedermanmikropul.com/en/knowledge-center/dealing-with-moisture-in-air-inlet-filtration-systems

57. S.-K. Moon, I. W. Cheong, S.-W. Cho, Effect of flow rates of the continuous phase on droplet size in dripping and jetting regimes in a simple fluidic device for coaxial flow, Colloids and Surfaces A: Physicochemical and Engineering Aspects, 454(2012), 84-88.

58. https://www.fluigent.com/product/microfluidic-components/droplet-starter-pack/

59. https://www.micronit.com/

60. https://www.microfluidic-chipshop.com/catalogue/microfluidic-chips/glass-chips/

61. http://www.rbs-cp.be/en/products.html?rbs_id=13

62. R. Homma, B. J. Baker, L. Jin, O. Garaschuk, A. Konnerth, L. B. Cohen, & D. Zecevic, Wide-field and two-photon imaging of brain activity with voltage- and calcium-sensitive dyes, Philosophical transactions of the Royal Society of London. Series B, Biological sciences, 364 (2009) 2453-67.

63. N. Aseyev, M.Roschine, V. N. Lerusalimsky, P. M. Balaban, and E. S. Nikitin, Biolistic delivery of voltage-sensitive dyes for fast recording of membrane potential changes in individual neurons in rat brain slices, Journal of Neuroscience methods, 212 (2013) 17-27.

64. J.-Y. Wu, X. Huang, and C. Zhang, Propagating Waves of Activity in the Neocortex: What They Are, What They do, The Neuroscientist, 14 (2008) 487-502.

65. S. Habib-e-rasul Mullah, R. Komuro, P. Yan, S. Hayashi, M. Inaji Y. Momose-Sato, L. M. Loew, K. Sato, Evaluation of voltage-sensitive fluorescence dyes for monitoring neuronal activity in the embryonic central nervous system, The Journal of Membrane Biology, 246 (2013) 679-88.

66. M. Manzo and O. Cavazos, Neurotransducers Based Voltage Sensitive Dye-Doped Microlasers, Optical Society of America :Biophotonics Congress (2019).

67. D. D. D'Lima, B. J. Fregly, and C. W. Colwell, Implantable sensor technology: measuring bone joint biomechanics of daily life in vivo, Arthritis Research & Therapy, 15 (2014).

68. T. Miclau, C. Lu, Z. Thompson, P. Choi, C. Puttlitz, R. Marcucio, and J. A. Helms, Effects of Delayed Stabilization on Fracture Healing, Journal of Orthopedic Research, 25 (2007) 1552–1558.

69. R. Schmidhammer, S. Zandieh, R. Hopf, I. Mizner, L. E. Pelinka, A. Kroepfl, and H. Redl, Alleviated Tension at the Repair Site Enhances Functional Regeneration: The Effect of Full Range of Motion Mobilization on the Regeneration of Peripheral nerves—Histologic, Electrophysiologic, and Functional Results in a Rat Model, Journal of Trauma and Acute Care Surgery, 56 (2004) 571–584.

70. K. Stoffel, K. Klaue, and S. M. Perren, Functional Load of Plates in Fracture Fixation in Vivo and Its Correlate in Bone Healing, Injury, 31 (2000).

71. K. C. McGilvray, E. Unal, K. L. Troyer, B. G. Santoni, R. H. Palmer, J. T. Easley, H. V. Demir, and C. M. Puttlitz, Implantable Microelectromechanical Sensors for Diagnostic Monitoring and Post-Surgical Prediction of Bone Fracture Healing," Journal of Orthopedic Research, 33 (2015) 1439–1446.

72. R. Chen, V. D. Ta, H. Sun, Bending-Induced Bidirectional Tuning of Whispering Gallery Mode Lasing from Flexible Polymers, ACS Photonics , 1 (2014) 11-16.

73. C.-W. Wu, C.-T. Chen, and C.-C. Chiang, A novel U-shaped, packaged, and microchanneled optical fiber strain sensor based on macro-bending induced whispering gallery mode, Sensors and Actuators A: Physical, 288 (2019) 86-91.

74. M. Himmelhaus, and A. Francois, In-vitro sensing of biomechanical forces in live cells by a whispering gallery mode biosensor, Biosensors and Bioelectronics, 25 (2009) 418-427.

75. S. A. Go, E. R. Jensen, S. M. O'Connor, L. Q. Evertz, D. A. Morrow, S. R. Ward, R. L. Lieber, and K. R. Kaufman, Design Considerations of a Fiber Optic Pressure Sensor Protective Housing for Intramuscular Pressure Measurements, Annals of Biomedical Engineering, 45 (2017) 739–746.

76. H. Alemohammad, 10 - Fiber Optical Sensors in Biomechanics, Opto-Mechanical Fiber Optic Sensors, Butterworth-Heinemann, (2018) 263–300.

77. S. A. Go, W. J. Litchy, L. Q. Evertz, and K. R. Kaufman, Evaluating Skeletal Muscle Electromechanical Delay with Intramuscular Pressure, Journal of Biomechanics, 76 (2018) 181–188.

78. A. Ramos, M. W. Schiller, I. Abe, P. A. Lopes, J. A. Simões, Experimental Measurement and Numerical Validation of Bone Cement Mantle Strains of an In Vitro Hip Replacement Using Optical FBG Sensors, Experimental Mechanics, 52 (2012) 1267-1274.

79. W. Kam, K. O'Sullivan, M. O'Keeffe, S. O'Keefe, W. S. Mohammed, and E. Lewis, Low cost portable 3-D printed optical fiber sensor for real-time monitoring of lower back bending," Sensors and Actuators A: Physical, 265 (2017)193-201.

80. R.G. Budynas, J.K., Nisbett, and J.E. Shigley, Shigley's mechanical engineering design, McGraw-Hill, New York, NY, (2011).